



**Michigan  
Technological  
University**



# **Richard and Elizabeth Henes Endowed Professor in Wind Energy**

**AY 2022/2023 Annual Report**

**Fernando Ponta**

**December, 2023**

## **Table of Contents:**

1. Introduction
2. Personnel Involved and Publications' List
3. Theoretical Background: Brief Description of CODEF and the GVLM Module
  - 3.1. The Common ODE Framework (CODEF) Multiphysics Model for Wind Turbine/Wind Farm Dynamics, and its Modules
  - 3.2. The Generalized Timoshenko Beam Model (GTBM)
  - 3.3. The DRD-BEM model
  - 3.4. The Gaussian-Core Vortex-Lattice Model (GVLM)
4. Research: MTU Simulation of the SNL-NRT Rotor Wake and Aeroelastic Dynamics
  - 4.1. First Stage - Project Objectives, Suggested Approach, and Preliminary Results
  - 4.2. Second Stage - Refinement of Blade Geometry and Internal Structure, and Simulations of its Aeroelastic Behavior
  - 4.3. Third Stage - Flexible Variations of the NRT Blade, their Aeroelastic Behavior, Wake Structure, and Velocity Patters
5. Concluding Remarks

## 1. Introduction

During this reporting period, the Richard and Elizabeth Henes Endowed Associated Professorship in Wind Energy provided graduate student support and equipment needs for the continued development of research in the area of advanced simulation and analysis of the aeroelastic dynamics of wind turbine rotors, and in particular, their interaction with other turbines within the wind farm collective.

In the previous phases of this project, we have leveraged on our wind turbine/wind farm codes R&D program at Michigan Tech University to expand the novel multiphysics computationally-efficient capabilities of the Common ODE Framework model (CODEF) to include a high-fidelity, moderate-order flow model for the farm collective called the Gaussian Vortex Lattice Model (GVLM).

In a collaborative research effort with Sandia National Labs under contract PO-2074866, an extensive series of simulations were conducted on the wake and aeroelastic dynamics of the next generation of light-weight high-speed rotors, implemented as part of SNL's National Rotor Testbed (NRT) program. The NRT program and DOE's Rotor Wake project as a whole were designing and preparing for a fiscal year 2023 experiment to investigate the interaction of highly flexible wind turbine blades and their wakes. Blades have continued to grow in length, and as they do their mass scaling factors have been going down to reduce the levelized cost of energy (LCOE). This has led to blades that are more prone to high tip deflections (as a percent of their length) and aeroelastic instabilities.

The Rotor Wake project directly benefited from simulations with the CODEF model because it specifically emphasizes the connection between blade flexibility and wake dynamics. CODEF models both the unsteady blade forces and motions, as well as the shed vorticity and wake of such a turbine. In order to help the Rotor Wake project planning future experiments, the following simulations, and questions to address, were proposed and investigated:

- How elastic must a blade be such that the average wake recovery and velocity deficit is significantly different than a rigid rotor at various downstream locations for various levels of turbulence and sheared inflow?
- This will be addressed by starting simulations with a baseline-blade rotor configuration, then reducing the blade section stiffness for subsequent simulations, thereby allowing the effect of blade flexibility on the blade bending moments and on the turbine's wake characteristics to manifest itself.
- Greater flexibility of the rotor will cause an increase in the unsteady shedding of turbulence and vorticity, and will likely enhance faster mixing of momentum in the wake core. We will quantify this effect in these simulations.

The results from these experiments are reported here.

## 2. Personnel Involved and Publications' List

### Personnel:

#### **Dr. Fernando Ponta**

Richard and Elizabeth Henes Endowed Professor in Wind Energy  
MEEM Department, Michigan Technological University

#### **Apurva Baruah**

PhD Student - Graduate Research Assistant  
MEEM Department, Michigan Technological University

#### **Alayna Farrell**

PhD Student - Graduate Research Assistant  
MEEM Department, Michigan Technological University

#### **North Yates**

PhD Student - Graduate Research Assistant.  
Work on the aeroelastic and blade vibrational dynamics aspects of the project.

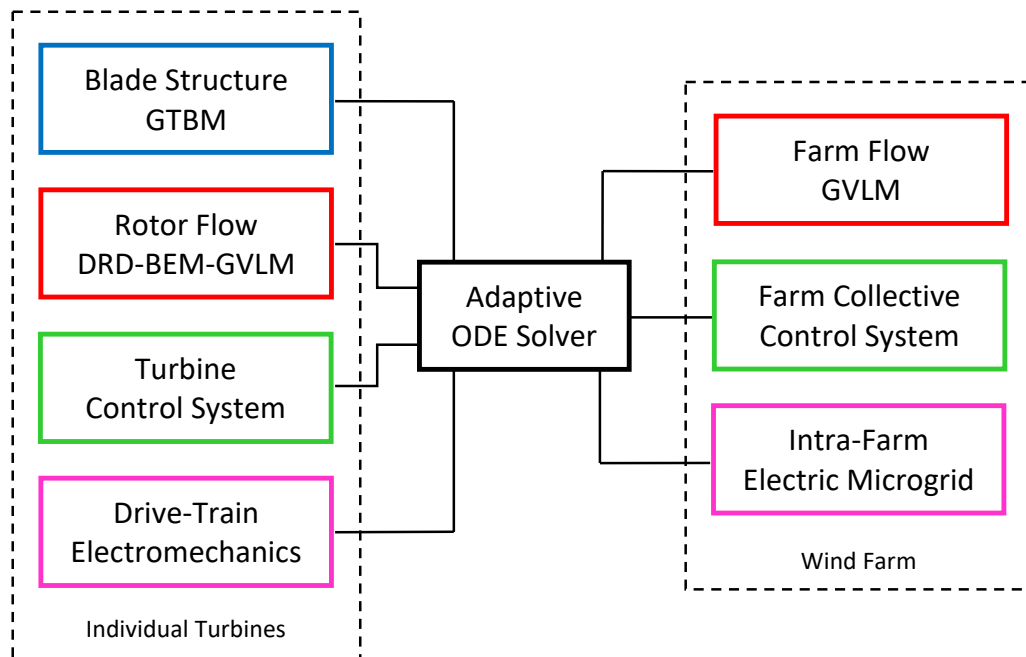
### Publications' List:

- [1] F. Ponta, A. Baruah, A. Farrell (2023); "Development of Reduced Order Models (ROMs) Representative of Wind Turbine Interaction: Phase 5 - Simulation of the Wake and Aeroelastic Dynamics of the SNL-NRT Rotor under Realistic Atmospheric Wind Conditions, and in a Waked Twin-Turbine Tandem Layout"; *Technical Report Sandia National Labs Contract PO-2074866-(4)*.
- [2] M. Menon, F. Ponta (2022); "Aerodynamic Flow Control on Wind Turbine Blades using Slotted Flaps"; *Fluids*, MDPI; Vol. (7), 129, 1-27.
- [3] F. Ponta, A. Baruah, A. Farrell (2022); "Development of Reduced Order Models (ROMs) Representative of Wind Turbine Interaction: Phase 4 - Simulation of the SNL-NRT Rotor Wake and Aeroelastic Dynamics"; *Technical Report Sandia National Labs Contract PO-2074866-(3)*.

### 3. Theoretical Background: Brief Description of CODEF, and the GVLM Module

#### 3.1. The CODEF Multiphysics Model for Wind Turbine/Wind Farm Dynamics, and its Modules

CODEF is an Adaptive Dynamic Multiphysics modeling technique for wind turbine dynamics via a Multivariable ODE Solution in time. Based on using non-linear adaptive variable-timestep /variable-order algorithms to solve a master ODE system, CODEF gathers together the equations associated with the different modules modeling rotor flow, blade structure, control system, and electromechanical devices (see Fig. 1-3.1). By monitoring the local truncation error at every timestep, CODEF provides a natural way of integrating, simultaneously, all aspects of the multiphysics problem, thereby improving computational efficiency and ensuring the stability of the time-marching scheme. These unique features make CODEF capable of modeling the aeroelastic dynamics associated with active control actions. Moreover, the CODEF's ODE system could be expanded to interface with the equations simulating the electrical interaction within the intra-farm microgrid, the wind-farm collective control system, and the farm-scale collective flow through the GVLM module, detailed next.



GTBM: Generalized Timoshenko Beam Model  
DRD-BEM: Dynamic Rotor Deformation - Blade Element Momentum  
GVLM: Gaussian Vortex Lattice Model

**Fig. 1-3.1:** Block schematics of CODEF, including its expansion to wind farm simulation.

Detailed description of CODEF key modules:

1. Moderate-Order High Fidelity Blade Structural Model: The Generalized Timoshenko Beam Model (GTBM) technique allows for a reduction of the 3D structural problem through a set of 2-D linear pre-resolutions on blade sections along the span into a 1-D, non-linear, time-dependent solution on an equivalent beam written as an ODE system. A brief description of the GTBM technique is provided in **Sec 3.2**, full details could be found in Ponta, et al. [1], Otero and Ponta [2], and references within.

2. Moderate-Order High Fidelity Rotor Flow Model: The Dynamic Rotor Deformation - Blade Element Momentum technique (DRD-BEM) provides a fully-coupled aero-elastic model based on a complete reformulation of the BEM technique including all the effects of dynamic rotor deformation via coupling with GTBM. In its initial form, the DRD-BEM was developed as a multiphysics model for an individual turbine (see Ponta, et al. [1]). However, it was also designed to interface with the farm-scale collective flow through integration with other numerical techniques, like the GVLM explained below. A brief description of the DRD-BEM is provided in **Sec 3.3**.

3. Moderate-Order High-Fidelity Collective Farm-Flow Model: The Gaussian-Core Vortex-Lattice Model (GVLM) is a high-fidelity alternative for farm collective flow-field simulation, with a moderate computational cost. GVLM consists of an ensemble of the individual Gaussian-core vortex filaments on the lattices generated by all turbines in the farm. The ensemble is shared by the collective Farm-Flow GVLM and by all the DRD-BE-GVLMs of the individual turbines. Gaussian distribution of vorticity in the vortex core accounts for the natural viscous decay of vortex filaments, freeing the memory from vortices that have already dissipated. This substantially reduces the computational cost versus classic vortex models based on the singularity concentration of vorticity in vortex filaments that never decay. It also provides a much more realistic representation of the interaction of vortices in close proximity, by avoiding the unrealistic, extremely high values of vortex-filament induced velocity given by the Biot-Savart law. Detailed descriptions of the Vortex-Lattice technique found in Ponta and Jacovkis [3] and Strickland, et al. [4]; details about the Gaussian-Core Vortex theory could be found in Ponta [5], and references within. A brief description of the GVLM formulation is also provided in **Sec 3.4**.

4. Modular Multiphysics Interface: CODEF is integration-ready with ODE modules modeling the dynamics of the electro-mechanical devices and the control system at the individual-turbine scale, as well as with expansions to include ODE equations modeling the electrical interaction within the intra-farm microgrid and the wind-farm collective control system.

### **3.2 The Generalized Timoshenko Beam Model**

GTBM uses the same variables of classical Timoshenko beam theory, but the hypothesis of beam sections remaining planar is abandoned. Instead, the real warping of the deformed section is interpolated by a 2-D finite-element mesh (see **Fig. 1-3.2** and **Fig. 2-3.2**). Then, the 3-D strain energy is rewritten in terms of the classical 1-D variables, and pre-solved. This dimensional reduction produces a fully populated 6x6 stiffness matrix for an equivalent beam, which includes all coupled-deformation modes, like the bending-twist mode. It allows the accurate modeling of the blade structural dynamics as a 1-D finite-element problem to be solved at each time-step of the ODE solution at a reduced computational cost (see **Fig. 3-3.2**).

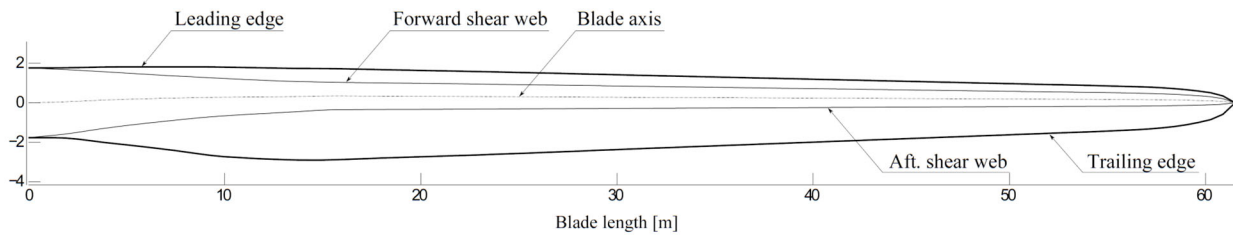


**Fig. 1-3.2:** Example of a typical blade design used in current commercial turbines.

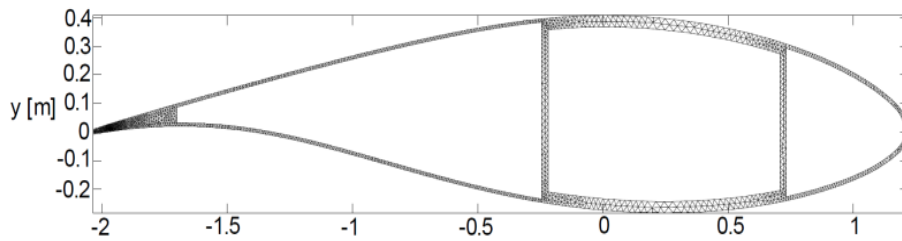


**Fig. 2-3.2:** Example of finite-element 2-D meshing of the internal structure of one of the blade sections used on the dimensional-reduction computations.

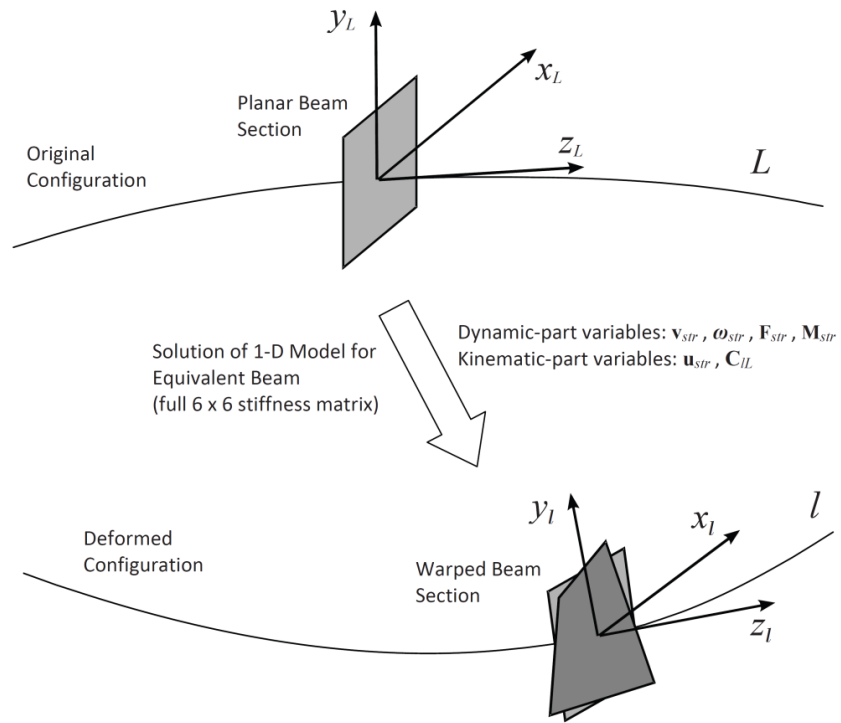


**Fig. 3-3.2:** Schematic representation of the GTBM finite-element solution for the equivalent beam 1-D model.

### 3.3 The Dynamic Rotor Deformation - Blade Element Momentum Model

In the DRD-BEM, the incoming wind velocity in the ground reference system,  $\mathbf{W}_{\infty wind}$ , is transformed through a series of orthogonal-matrix linear operators to give the velocity vector in the system of coordinates of the blade section in its instantaneous deformed configuration,  $\mathbf{W}_l$ . This technique fully includes the effects of the misalignments induced by large rotations of the airfoil sections due to blade deformation on the computation of the aerodynamic forces acting on each blade element. It also includes misalignments induced by the action of mechanisms like yaw, pitch, main-shaft rotation; by blade design features like twist, pre-bending and sweep; and by rotor's design features like tilt or coning. **Fig. 1-3.3** schematizes the coordinate transformation process.

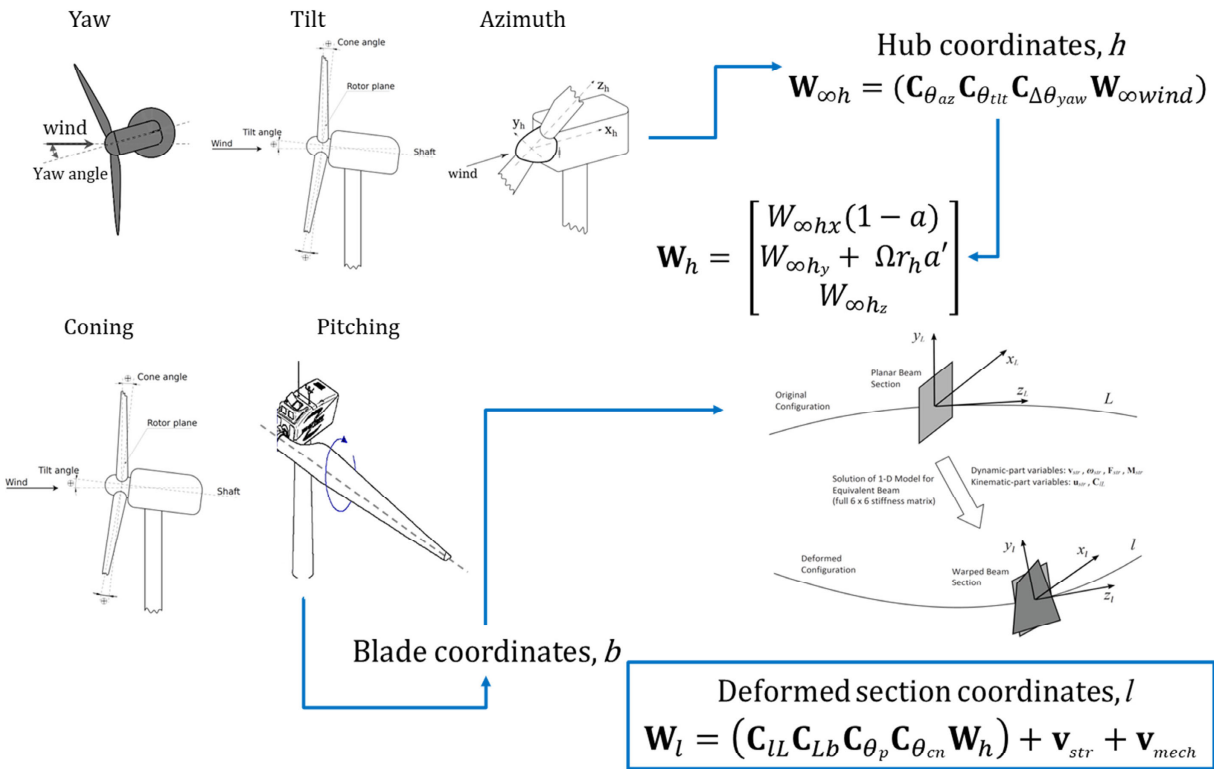


**Fig. 1-3.3:** Schematic representation of the DRD-BEM coordinate transformations for the projection of velocities and forces by orthogonal-matrix linear operators.

An example of orthogonal-matrix linear operator to account for pitch-control actuation:

$$\mathbf{C}_{\theta_p} = \begin{bmatrix} \cos(-\theta_p) & \sin(-\theta_p) & 0 \\ -\sin(-\theta_p) & \cos(-\theta_p) & 0 \\ 0 & 0 & 1 \end{bmatrix}$$



Once the wind velocity in the hub coordinate system,  $\mathbf{W}_h$ , is modified to account for interference by application of the axial and angular velocity-induction coefficients  $a$  and  $a'$ , is then transformed into the blade section coordinates. Here, velocity components due to structural vibration,  $\mathbf{v}_{str}$ , and the action of mechanisms,  $\mathbf{v}_{mech}$ , are added.

$$\mathbf{W}_{\infty h} = (\mathbf{C}_{\theta_{az}} \mathbf{C}_{\theta_{tit}} \mathbf{C}_{\Delta\theta_{yaw}} \mathbf{W}_{\infty wind})$$

$$\mathbf{W}_h = \begin{bmatrix} W_{\infty h_x} (1 - a) \\ W_{\infty h_y} + \Omega r_h a' \\ W_{\infty h_z} \end{bmatrix}$$

$$\mathbf{W}_l = (\mathbf{C}_{LL} \mathbf{C}_{Lb} \mathbf{C}_{\theta_p} \mathbf{C}_{\theta_{cn}} \mathbf{W}_h) + \mathbf{v}_{str} + \mathbf{v}_{mech}$$

Aerodynamic forces on the blade sections are computed and transformed back to the stream-tube in the hub coordinates to obtain the interference factors via the BEM technique:

$$\delta \mathbf{F}_h = \mathbf{C}_{\theta_{cn}}^T \mathbf{C}_{\theta_p}^T \mathbf{C}_{Lb}^T \mathbf{C}_{LL}^T \mathbf{C}_{Lthal} \mathbf{dF}_{rel} \delta l$$

The aerodynamic forces on the blade sections are also used as input to the GTBM structural model. Full details about DRD-BEM's mathematical derivations and other aspects could be found in Ponta, et al. [1].

### 3.4 The Gaussian-Core Vortex-Lattice Model

The GVLM is a high-fidelity alternative for farm collective flow-field simulation, with moderate computational cost. It could be combined with the DRD-BEM technique to produce a model for the global farm flow which is economical in terms of computational cost, but still highly accurate in representing vortex wake structure evolution and meandering (and their effect in turbine-to-turbine interaction).

There are two key features that make this Gaussian-core VLM much more realistic and stable than previous VLMs based on the Biot-Savart law:

- i. The first is related with the natural representation of the viscous decay of vortex "filaments" due to the Gaussian distribution of vorticity in their cores (versus the simple filament-singularity concentration of the Biot-Savart law), which allows a realistic representation of vortex-induced velocities along the wake's lifespan. It also allows the freeing of computer memory from vortices that have already "dissipated".
- ii. The second is that it avoids the problem of high-speed vortex mutual "satellisation" occurring when two vortex filaments enter into close proximity. This is due to the unrealistically high value of tangential velocity in the close vicinity of the filament caused, again, by the concentration of vorticity on the Biot-Savart law filament-singularity, and its hyperbolic distribution of tangential velocity. This unique characteristic also allows for a remarkable stability of the vortex lattice, which enables GVLM to extend very long distances downstream of the rotor.

The following schematics are intended to summarize the basic principles behind GVLM:

**Fig. 1-3.4** shows a plot of the vorticity and tangential velocity distributions on a generic Gaussian-core vortex filament.

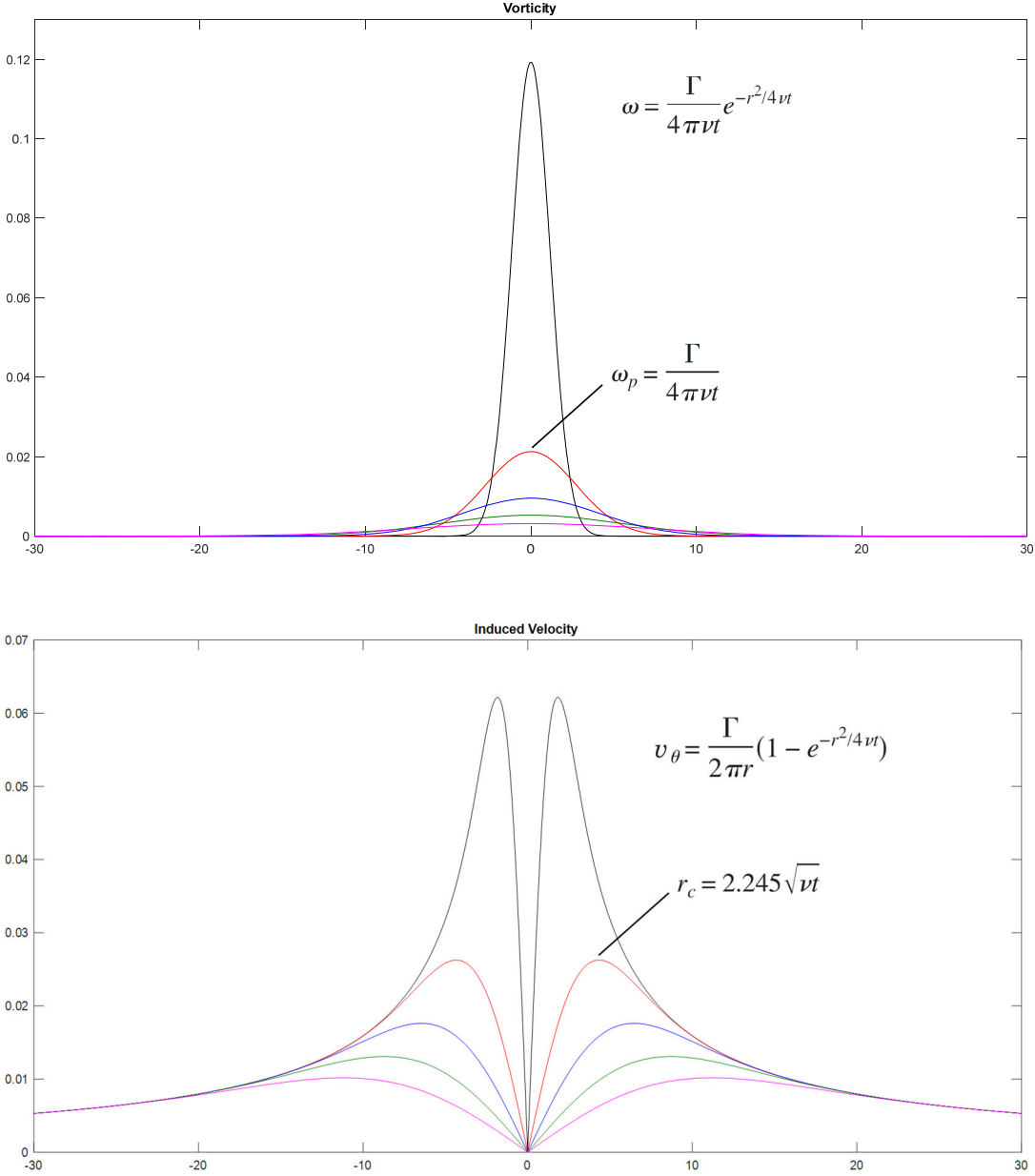


**Fig. 1-3.4:** Vorticity and induced tangential velocity distributions on a generic Gaussian-core vortex filament.

**Fig. 2-3.4** briefly summarizes some basic principles from the original studies of Gaussian-core vortex dynamics in the context of Karman vortex-street wakes presented in Ponta [5]. These built up on a series of previous works on vortex generation by shear-layer roll up and vortex shedding (Ponta and Aref [6]); and on the further vortex evolution until a homogeneous, stable vortex core is formed (Ponta [7]).

**Fig. 3-3.4**, briefly summarizes some basic principles of the vortex-lattice technique implemented in Ponta and Jacovkis [3], which evolves from the works of Strickland, et al. [4].

## The Gaussian-Core Vortex Model In the evolution of the Karman vortex street

“Vortex decay in the Karman eddy street” by Ponta, *Physics of Fluids*, 22, (2010): 093601.  
 “Analyzing the vortex dynamics in bluff-body wakes by Helmholtz decomposition of the velocity field” by Ponta, *Fluid Dynamics Research*, 38, (2006): 431–451.  
 “Strouhal-Reynolds number relationship for vortex streets” by Ponta and Aref, *Physical Review Letters*, 93, (2004): 084501.

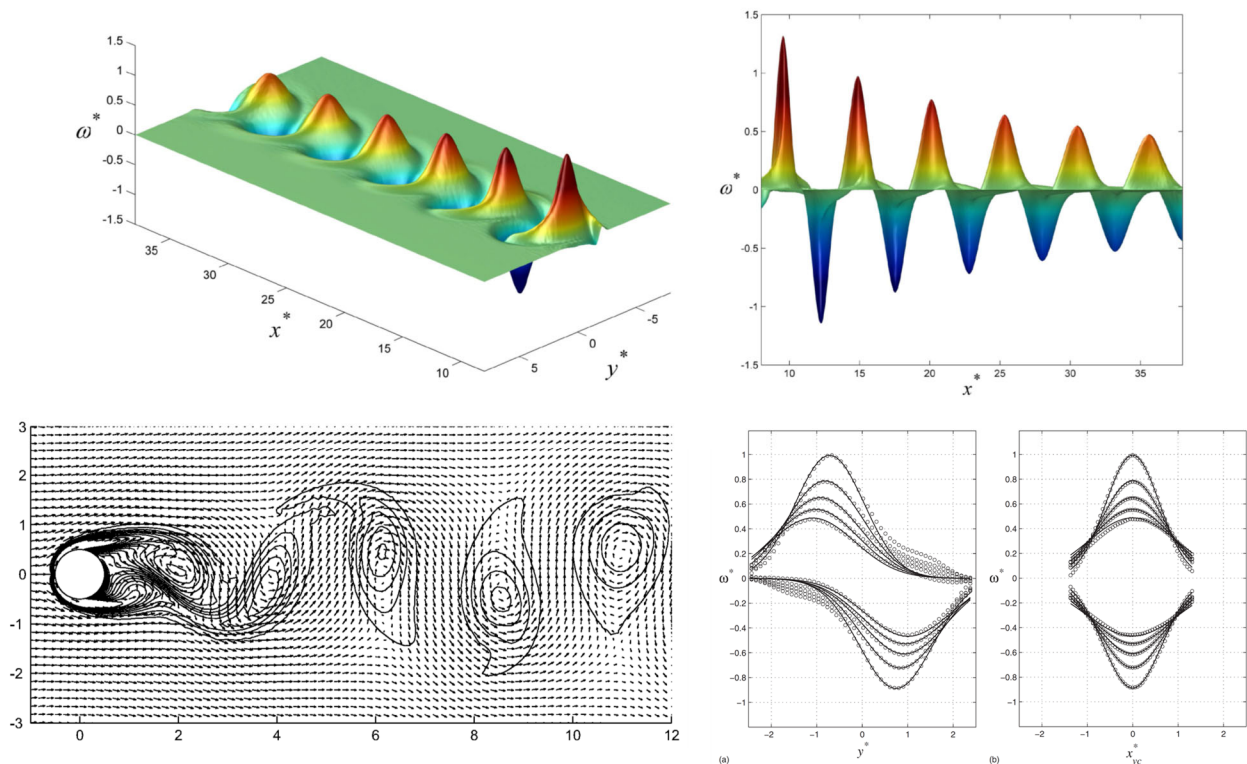
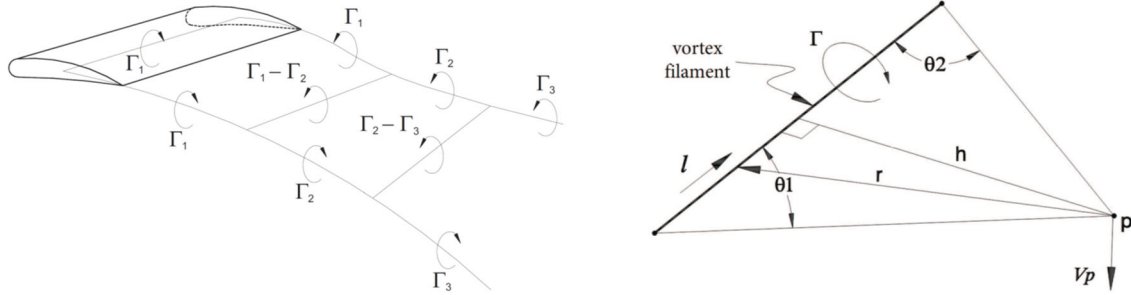


**Fig. 2-3.4:** Summary of some basic principles from the original studies on Gaussian-core vortex dynamics in the context of Karman vortex-street wakes (Ponta [5]), building up on a series of previous works on vortex generation and shedding (Ponta and Aref [6]), and on the evolution of stable vortex cores (Ponta [7]).

## The Gaussian-Core Vortex Model In the Vortex Lattice Technique

Implemented by Ponta and Jacovkis, "A vortex model for Darrieus turbine using finite element techniques", *Renewable Energy*, 24, (2001); evolved from "Vortex model of the Darrieus turbine: an analytical and experimental Study" by Strickland, Webster and Nguyen, *J. Fluid Engineering*, 101, (1979)



Classical implementation - Biot-Savart law

$$\mathbf{v}_p = \mathbf{e} \frac{\Gamma}{4\pi h} (\cos\theta_1 + \cos\theta_2)$$

GVLM implementation – Gaussian core vortex model

$$\mathbf{v}_p = \mathbf{e}_{v_p} \frac{\Gamma}{4\pi h} \left(1 - e^{-h^2/4\nu t}\right) (\cos\theta_1 + \cos\theta_2)$$

$$\Delta x(i, j) = \left[ \frac{3}{2} \mathbf{U}(i, j)_{t=t_{NT}} - \frac{1}{2} \mathbf{U}(i, j)_{t=t_{NT-1}} \right] \Delta t$$

**Fig. 3-3.4:** Schematic representation of the GVLM creation of a set of shed and trailing vortex filaments emanating from a blade element, a comparison of GVLM formula for induction of velocities versus the classic Biot-Savart law, and filament-nodal propagation by an Adams-Bashforth second order time-integration formula.

## **4. Research: MTU Simulation of the SNL-NRT Rotor Wake and Aeroelastic Dynamics**

After the discussion of the basic theoretical background in previous sections, this part of the present report will focus on the research efforts conducted to address the main objectives established in **Sec 1**. Even though the objectives are interrelated, for organizational purposes, this discussion will be divided in three Stages, corresponding to each one of the following sections.

### **4.1 First Stage - Project Objectives, Suggested Approach, and Preliminary Results**

In this section, we shall discuss the initial steps of the First Stage of the research efforts, which were focused on the conversion of the NRT-Baseline blade data, shared by SNL, into MTU's multiphysics CODEF format, and the development of flexible blade variations that had their spar-caps reduced by 80% and 90%. This was followed by a preliminary series of results obtained for the aeroelastic oscillatory response of the three blades.

#### **Project Objectives to Address:**

- How flexible do wind turbine blades need to be to change the character of the wake?
- Under what atmospheric and turbine conditions does blade flexibility change the wake? (WS, TI, shear, yaw)

#### **Initial Approach:**

- Load NRT Blade design from FAST and Ansys models and convert to MTU input format
- Simulate NRT rotor and wake for baseline test matrix conditions
- Quantify blade loads: root bending moment and tip deflection
- Quantify wake: axial velocity up to 5 diameters (5D) downstream of the turbine in 1D increments
- Increase NRT blade flexibility
- For example, reduce spar cap thickness 10%, and note the change in flap-wise stiffness ( $EI_{flap}$ ), edgewise stiffness ( $EI_{edge}$ ), torsional stiffness ( $GJ_{torsion}$ ), and blade mass distribution
- Repeat simulations and analysis for more flexible blades

#### **Test Matrix Simulation Features:**

- This test matrix is intended to serve as a guide to facilitate answering the objectives
- Pairs of TI/shear are representative of day and night conditions at SWiFT
- Yaw offset conditions are assumed to be either 0- or 10-degrees

- NRT.90 is 90% spar cap thickness of baseline
- NRT.80 is 80% spar cap thickness of baseline
- 80 and 90 can be changed if we are not seeing differences in wake velocities
- Test-matrix cases are summarized in **Table 1-4.1** below

| Simulation # | Blade  | Tl (%) | Shear Exponent | WS (m/s) | TSR | Yaw (deg) |
|--------------|--------|--------|----------------|----------|-----|-----------|
| 1            | NRT    | 18     | 0.06           | 6        | 9   | 0         |
| 2            | NRT    | 18     | 0.06           | 6        | 9   | 10        |
| 3            | NRT    | 8      | 0.30           | 6        | 9   | 0         |
| 4            | NRT    | 8      | 0.30           | 6        | 9   | 10        |
| 5            | NRT.90 | 18     | 0.06           | 6        | 9   | 0         |
| 6            | NRT.90 | 18     | 0.06           | 6        | 9   | 10        |
| 7            | NRT.90 | 8      | 0.30           | 6        | 9   | 0         |
| 8            | NRT.90 | 8      | 0.30           | 6        | 9   | 10        |
| 9            | NRT.80 | 18     | 0.06           | 6        | 9   | 0         |
| 10           | NRT.80 | 18     | 0.06           | 6        | 9   | 10        |
| 11           | NRT.80 | 8      | 0.30           | 6        | 9   | 0         |
| 12           | NRT.80 | 8      | 0.30           | 6        | 9   | 10        |

**Table 1-4.1:** Summary of characteristic parameters for three different operating scenarios studied in the suggested approach of the preliminary First Stage.

**First Stage - Progress Summary:**

- SNL shared NRT design package and FAST input files, and regular update meetings were set up, discussing details about geometry and internal structure characteristics of NRT blade
- Importing/converting to MTU format for the baseline NRT blade geometry was completed, and then internal structure 90% and 80% adjustment of spar cap thickness
- While work on structural-parameters conversion continued, preliminary vortex-wake simulations were conducted with an NRT-Geometry blade using a generic box-beam spar internal structure.
- The purpose was evaluating aerodynamic-geometry and TSR effects on vortex-shedding process (e.g., vortex filament intensity, filament shedding frequency, vortex lattice density, and Gaussian-cores turbulent diffusivity coefficient) to achieve the targeted objective of 10-diameter wake simulation, with proper resolution.
- Wind conditions listed on cases #1, and #3 on the Test Matrix were run on these preliminary tests, so as to compare the effects of wind profiles during typical nighttime and daytime periods. These show different patterns of behavior in terms of the interaction of the vortex wake with the

background wind profile affecting the evolution of wake shape. Images of wake structure are produced. A sample selection of these are included below.

- Preliminary simulations of the aeroelastic oscillatory behavior were run for the NRT Baseline blade, and for the 90% and 80% variations with thinner spar-caps.
- Plots were produced for the time evolution of several variables to illustrate the structural response when exposed to the nighttime and daytime flow patterns: Blade-tip deflection, torsional angle, and angle of attack a representative section; plus, power, torque and thrust at the hub. A sample selection of these are included below.
- These results were intended to serve as a basis for discussion about some operational parameters of the NRT rotor for the next stage of the project.

### Preliminary Vortex-Wake Simulations:

Vortex wake simulations were conducted in this initial stage for the NRT-geometry blade for wind conditions listed on Simulation #1 and Simulation #3 of the test matrix shown in **Table 1-4.1**. The case for Simulation #1 was tested with and without a 0.5-degree root-cut to evaluate the difference in vortex intensities. The case for Simulation #3 was only tested without a 0.5-degree root-cut.

A sample selection of those results is shown in **Fig. 1-4.1**, **Fig. 2-4.1**, **Fig. 3-4.1**, and **Fig. 4-4.1**. These figures show views of the vortex-lattice meshes produced by GVLM which serve to illustrate the vortex-wake structure. Perspective views are shown in **Fig. 1-4.1**, and **Fig. 3-4.1**, and **Fig. 2-4.1**, and **Fig. 4-4.1** show the wake cross-section cuts up to 5 diameters downstream of the turbine in increments of 1 diameter.

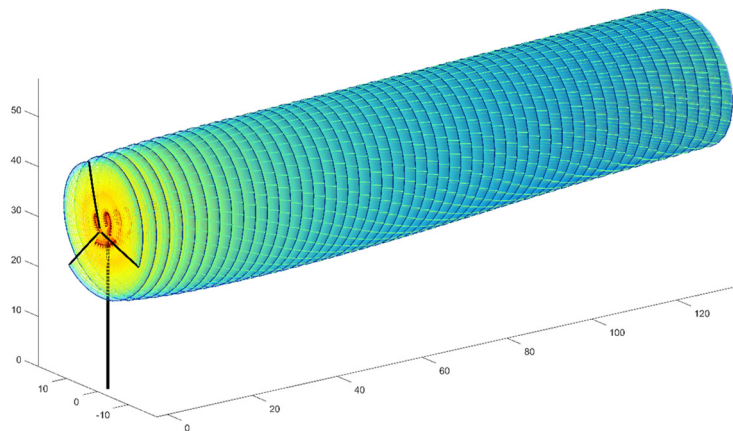


**Fig. 1-4.1:** Vortex filament intensity and vortex lattice shape shown in perspective up to 5D downstream of the turbine. Matrix Simulation #1, w/root cut, 6m/s, yaw offset = 0° and veer = 0°.

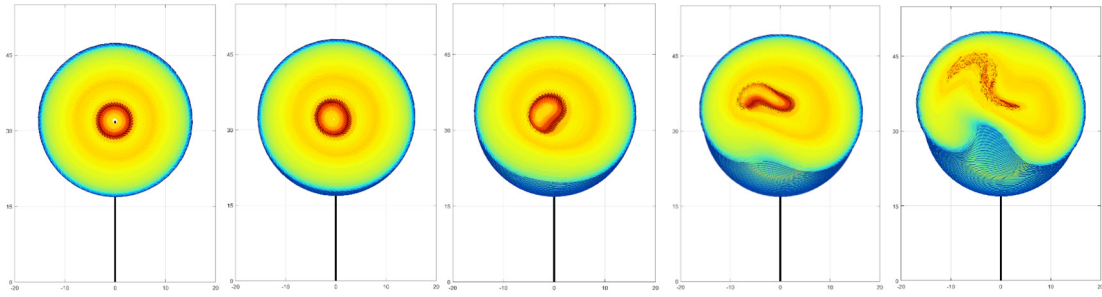


**Fig. 2-4.1:** Wake cross-section cuts plotted up to 5 diameters downstream in increments of 1 diameter from left to right. Matrix Simulation #1, w/root cut, 6m/s, yaw offset = 0° and veer = 0°.

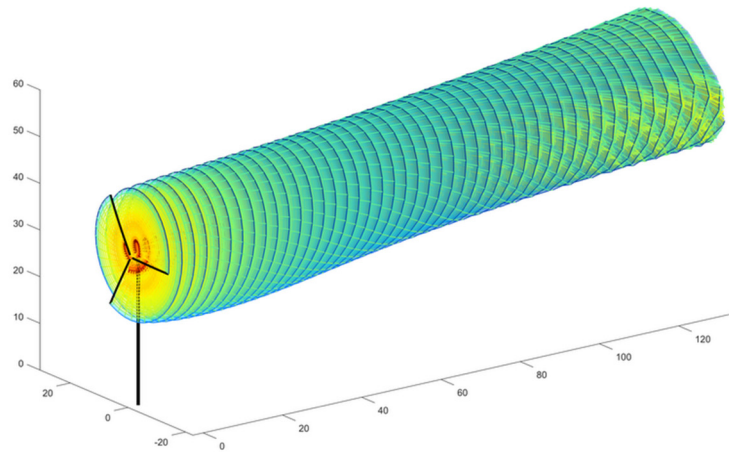


**Fig. 3-4.1:** Vortex filament intensity and vortex lattice shape shown in perspective up to 5D downstream of the turbine. Matrix Simulation #3, no root cut, 6m/s, yaw offset = 0° and veer = 0°.

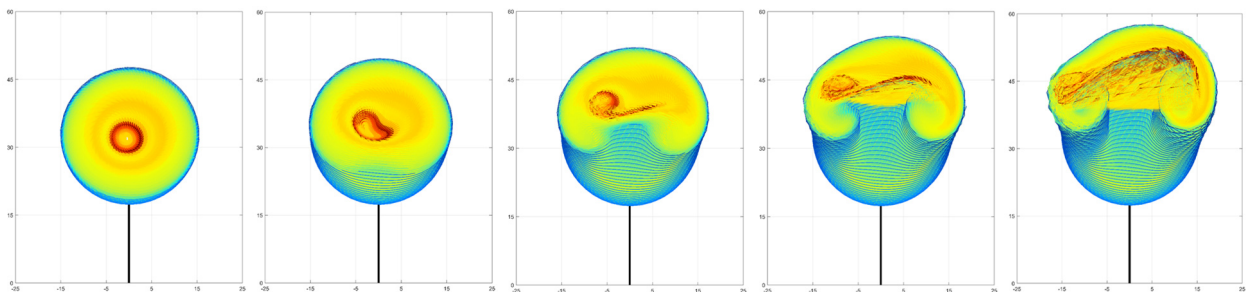


**Fig. 4-4.1:** Wake cross-section cuts plotted up to 5 diameters downstream in increments of 1 diameter from left to right. Matrix Simulation #3, no root cut, 6m/s, yaw offset = 0° and veer = 0°



### Preliminary Simulations of the Aeroelastic Oscillatory Behavior:

The aeroelastic oscillatory behavior for the NRT Baseline blade, and the 90% and 80% variations with thinner spar-caps, was tested.

Plots were produced for the time evolution of blade-tip deflection; plus, deflection torsional angle, and angle of attack at the section located at 90% of the blade span; plus, power, torque and thrust at the hub. A sample selection of those results is shown in **Fig. 5-4.1**, **Fig. 6-4.1**, and **Fig. 7-4.1**, for several wind conditions on the test matrix.

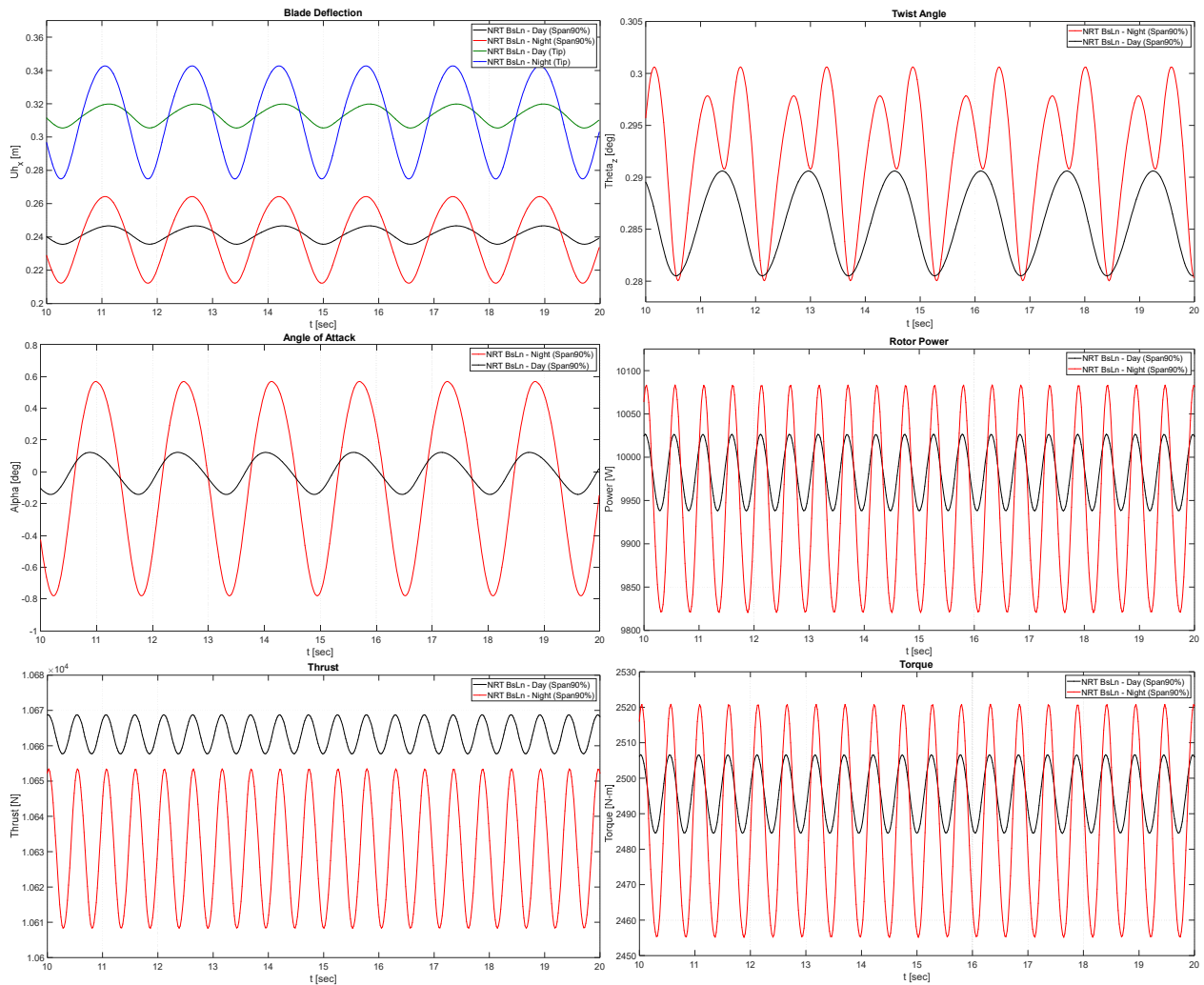


**Fig. 5-4.1:** Aeroelastic oscillatory behavior for Matrix Simulations #1 and #3, w/root cut: 6m/s, yaw offset = 0° and veer = 0°.

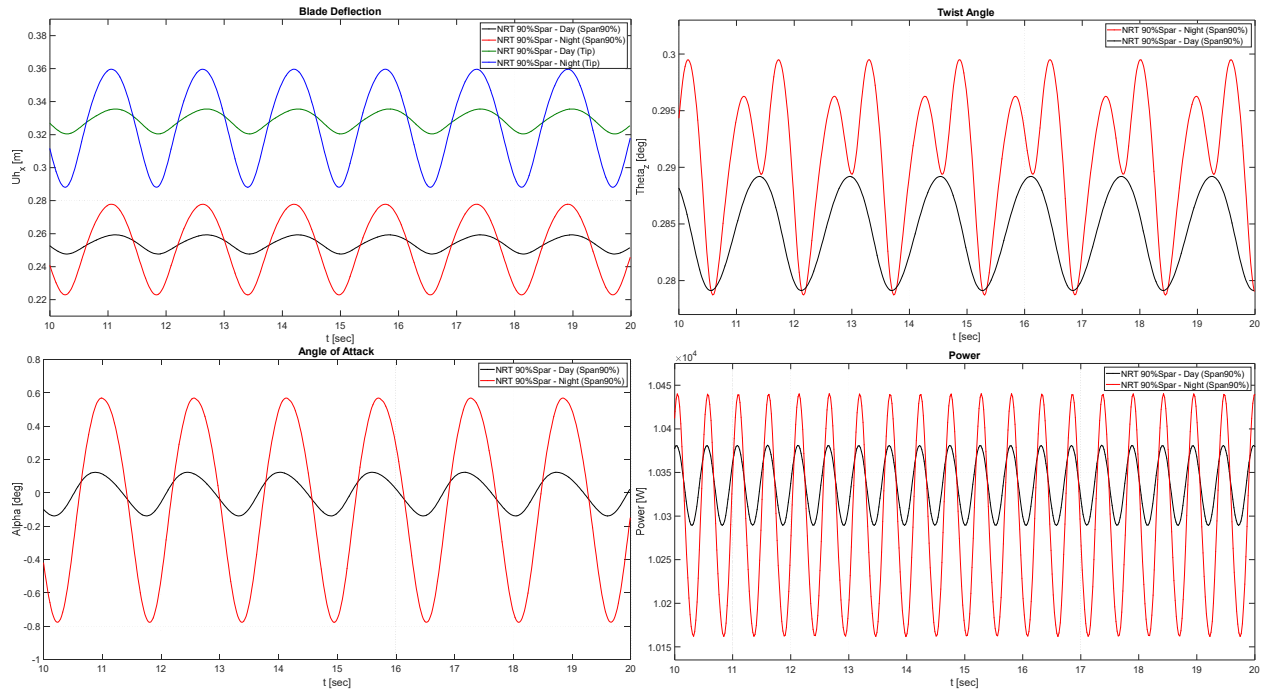


**Fig. 6-4.1:** Aeroelastic oscillatory behavior for Matrix Simulations #1 and #3, w/root cut: 6m/s, yaw offset =  $0^\circ$  and veer =  $0^\circ$

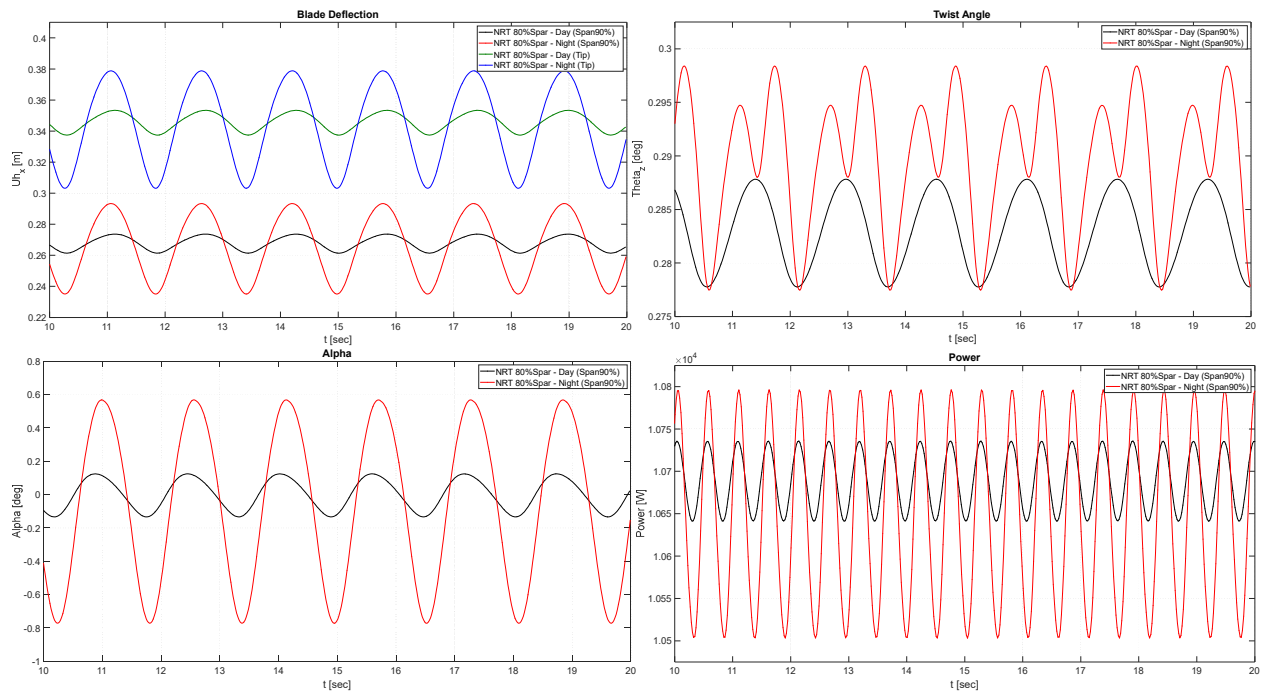


**Fig. 7-4.1:** Aeroelastic oscillatory behavior for Matrix Simulations #1 and #3, w/root cut: 6m/s, yaw offset =  $0^\circ$  and veer =  $0^\circ$

## 4.2 Second Stage - Refinement of Blade Geometry and Internal Structure, and Simulations of its Aeroelastic Behavior

In this section, we shall discuss the research work conducted on the Second Stage of the current phase of the project. From the preliminary results obtained in the First Stage, a complete revision of the materials and thicknesses of different components of the internal structure was conducted, exploring alternative ways of softening the blade by scaling the thicknesses of those components. Focus was given to the 80% thickness reductions to emphasize the effects of the contribution of different members of the internal structure, with the intention of exploring other percentage variations later on. The following variations were devised:

- (a - “BsLn”) Baseline Blade case,
- (b - “80Sp”) 80% adjustment of UNI spar cap material content,
- (c - “80Uni”) 80% of all UNI material (spar cap + shell),
- (d - “80Sh”) 80% all shell material, and
- (e - “80SpSh”) 80% all shell plus spar cap material

Span distributions of  $EI_{flap}$ ,  $EI_{edge}$ ,  $GJ_{torsion}$ , plus Blade mass distribution, were computed for the 80% flex variations. These are plotted in **Fig. 1-4.2**, compared with their Baseline counterparts.

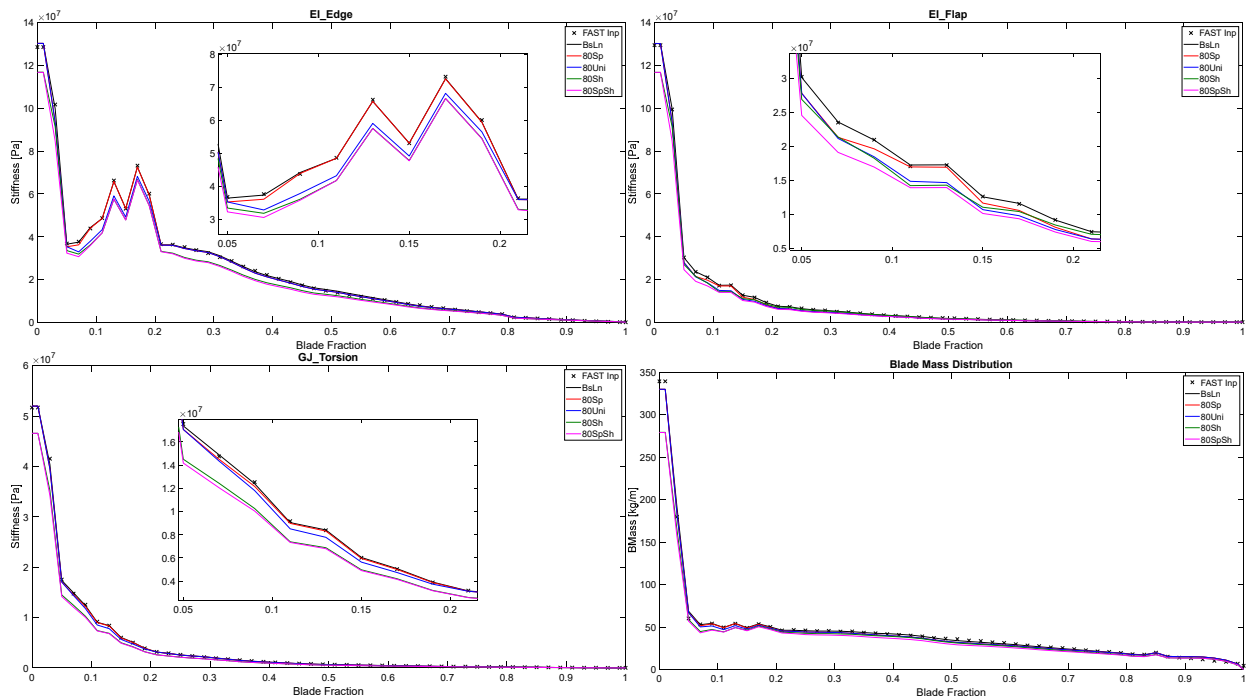


**Fig. 1-4.2:** Span distribution of Flap-wise, Edge-wise and Torsional stiffness, and Mass distribution, for the NRT Baseline blade and its 80% flex variations.

Preliminary simulations of the aeroelastic oscillatory behavior were ran for the NRT Baseline blade and its four 80% flex variations, operating at daytime and nighttime conditions, with and without yaw. Those correspond to the wind characteristics on cases #1 through #4, listed in the test matrix in Table 1-4.1, which will be referred henceforth as "Matrix Condition #1, #2, #3 or #4."

Plots were produced for the time evolution of several variables to illustrate the structural response when exposed to the daytime and then nighttime flow patterns. These results were intended to serve as a basis for discussion about construction and operational parameters of the NRT rotor for the next stage of the project. A sample selection of results for some relevant aeroelastic variables is shown in **Fig. 2-4.2**, **Fig. 3-4.2**, **Fig. 4-4.2**, and **Fig. 5-4.2**, for wind characteristics #1 through #4 in the test matrix.

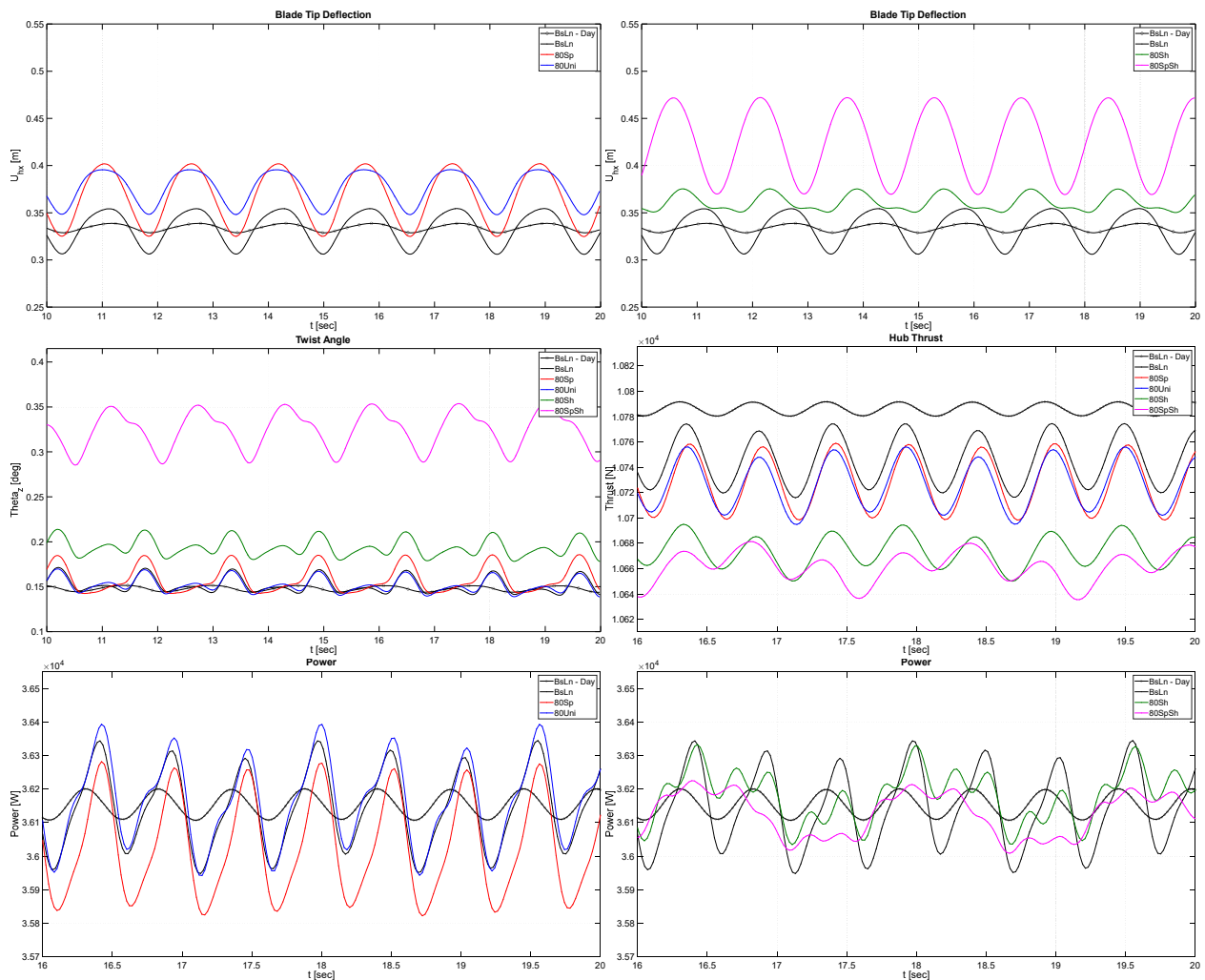


**Fig. 2-4.2:** Aeroelastic oscillatory behavior for the NRT Baseline blade, and 80% flex variations. Matrix Condition #3: Night, WS 6m/s, shear exp. = 0.30, yaw offset = 0°, TSR = 9, veer = 0°

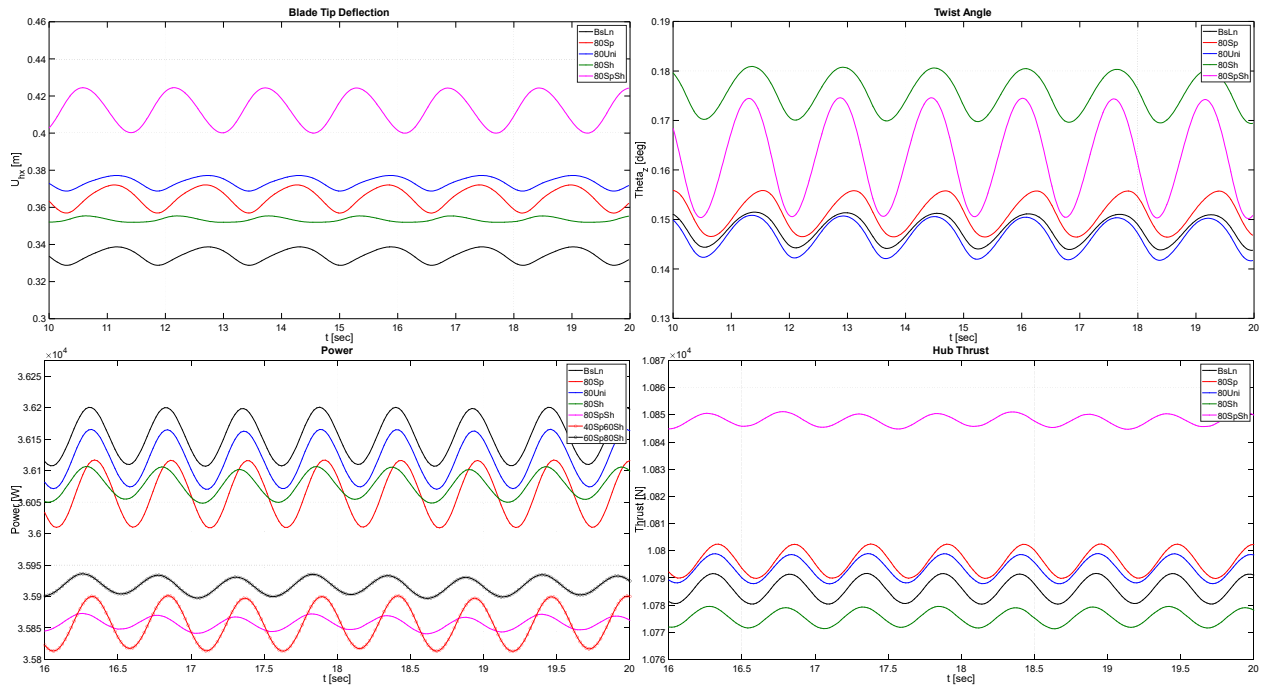


**Fig. 3-4.2:** Aeroelastic oscillatory behavior for the NRT Baseline blade, and 80% flex variations. Matrix Condition #1: Day, WS 6m/s, shear exp. = 0.06, yaw offset = 0°, TSR = 9, veer = 0°.

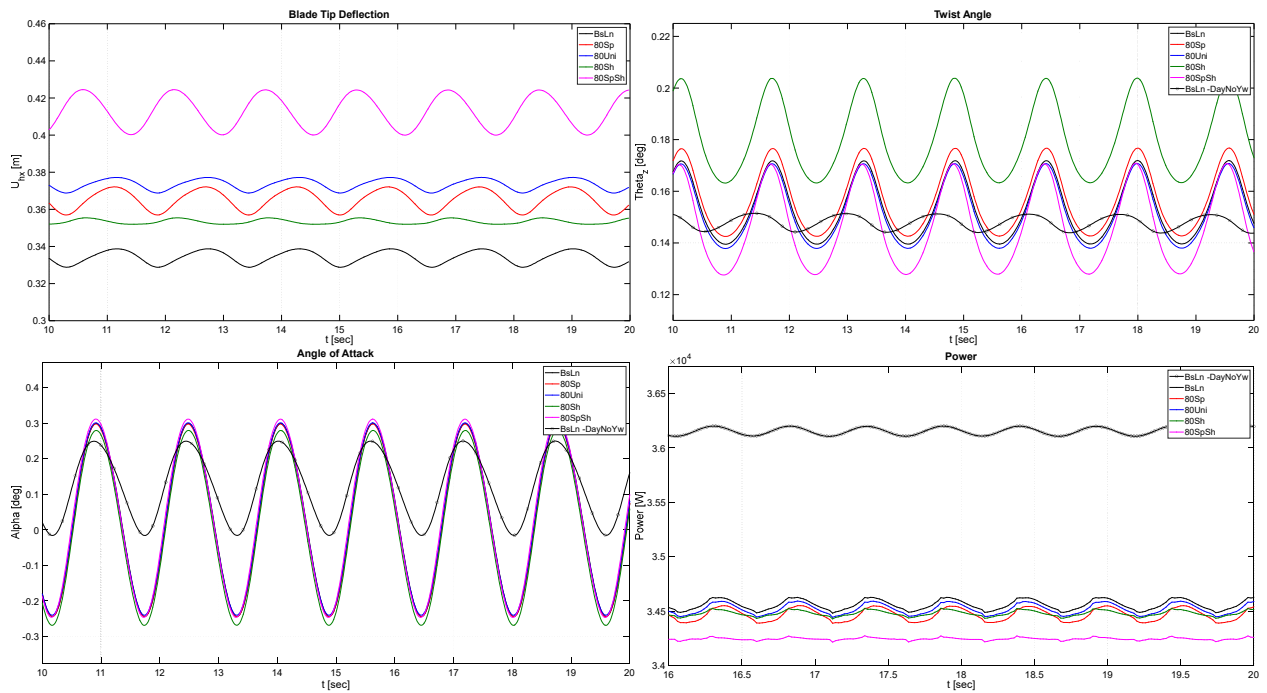


**Fig. 4-4.2:** Aeroelastic oscillatory behavior for the NRT Baseline blade, and 80% flex variations. Matrix Condition #2: Day, WS 6m/s, shear exp. = 0.06, yaw offset = 10°, TSR = 9, veer = 0°.

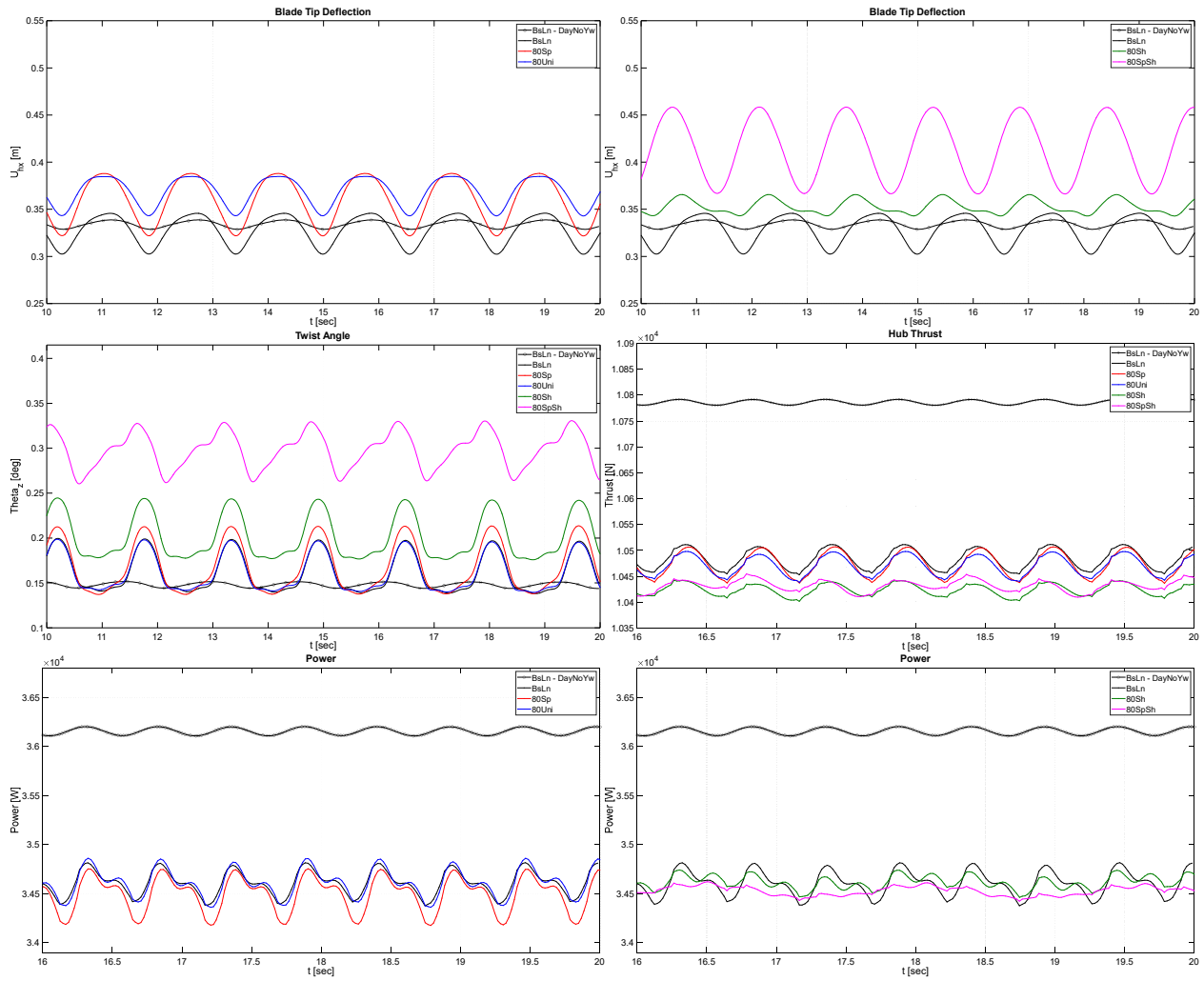


**Fig. 5-4.2:** Aeroelastic oscillatory behavior for the NRT Baseline blade, and 80% flex variations. Matrix Condition #4: Night, WS 6m/s, shear exp. = 0.30, yaw offset = 10°, TSR = 9, veer = 0°.

### 4.3 Third Stage – Additional Flexible Variations of the NRT Blade, their Aeroelastic Behavior, Wake Structure, and Velocity Patterns

In this section, we shall discuss the research work conducted during the Third Stage of the current phase of the project. Five new blade variations of increasing flexibility were created, combining different scaling factors for the spar cap and the shell thicknesses. Their aeroelastic response was analyzed in four different wind scenarios: daytime and nighttime, both with and without yaw. Vortex-lattice structure and wake velocity patterns for the three variations showing the most significant changes in aeroelastic response were also analyzed for two wind scenarios: daytime no-yaw, and nighttime with yaw. These represent the ends of the spectrum in terms of the cyclical variations that they induce in the aerodynamic loads. The difference in wake axial velocity between the baseline blade and each one of the three flexible variations were computed, normalized by the value of the incident wind.

The following variations of the NRT blade internal structure were created, to increase flexibility by scaling the thicknesses of the shell and the spar cap:

- (a - “BsLn”) Baseline Blade case,
- (b - “60%SpSh”) 60% shell and spar cap material,
- (c - “40%Sp-60%Sh”) 40% spar cap and 60% shell,
- (d - “40%SpSh”) 40% shell and spar cap material,
- (e - “20%Sp-40%Sh”) 20% spar cap and 40% shell, and
- (f - “20%SpSh”) 20% shell and spar cap material

Span distributions of  $EI_{flap}$ ,  $EI_{edge}$ ,  $GJ_{torsion}$ , and Blade mass distribution, were computed for the different flex variations. These are plotted in **Fig. 1-4.3**, compared with their Baseline counterparts. A table of total blade mass for each case is also shown in **Table 1-4.3**.

| Blade Variant | Mass [kg] | % vs BsLn |
|---------------|-----------|-----------|
| BsLn          | 551.156   | -         |
| 60% SpSh      | 360.594   | 65.42     |
| 40%Sp – 60%Sh | 344.8626  | 62.57     |
| 40% SpSh      | 260.4445  | 47.25     |
| 20%Sp – 40%Sh | 244.6009  | 44.38     |
| 20%SpSh       | 156.2864  | 28.35     |

**Table 1-4.3:** Total Blade Mass for the NRT Baseline blade and its flex variations.

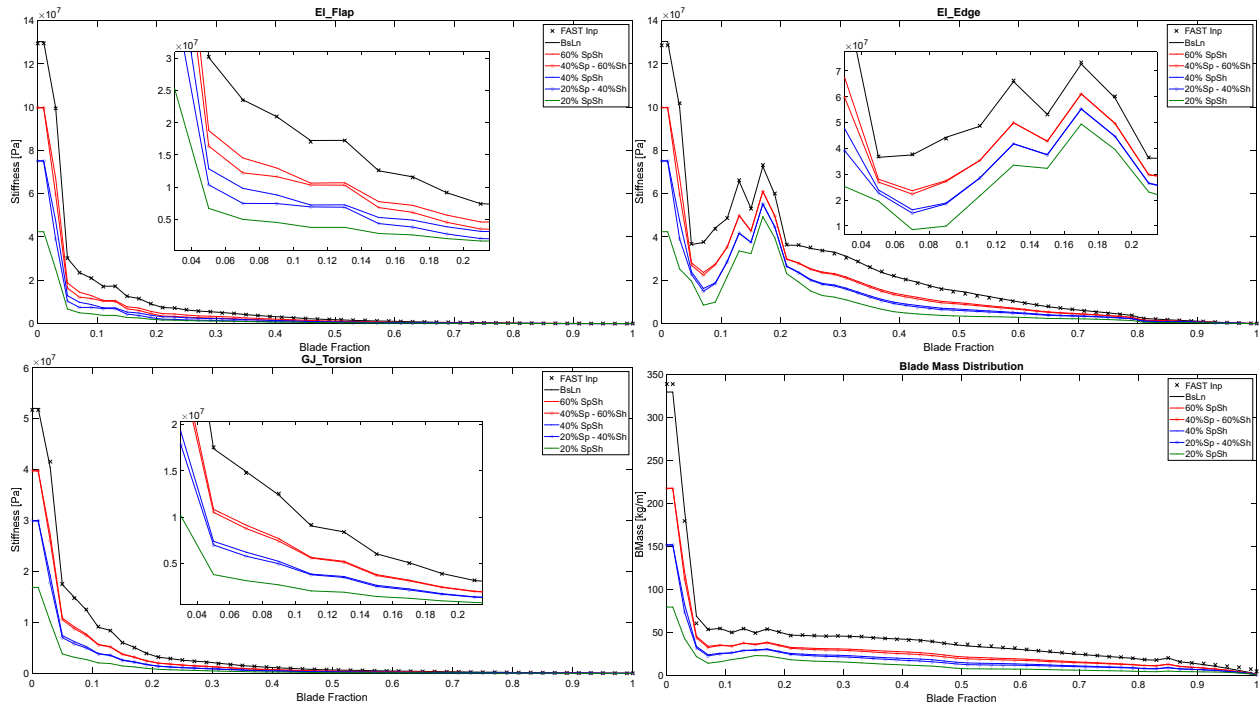


**Fig. 1-4.3:** Span distribution of Flap-wise, Edge-wise and Torsional stiffness, and Mass distribution, for the NRT Baseline blade and its flex variations

### Third Stage - Aeroelastic Oscillatory Behavior:

Simulations of the aeroelastic oscillatory behavior were run for the NRT Baseline blade and its different flex variations, operating at daytime and nighttime conditions, with and without yaw (i.e., wind characteristics #1 through #4 in the test matrix).

Plots were produced for the time evolution of several variables to illustrate the structural response when exposed to the daytime and nighttime flow patterns. Besides their usefulness in illustrating the structural response of the blade in its different flex variations, these results were intended to serve as a basis for selecting which were the case scenarios (in terms of wind operational conditions) that were likely to show the most significant changes in vortex wake structure and wake velocity patterns.

A sample selection of results for some relevant aeroelastic variables is shown in **Fig. 2-4.3**, **Fig. 3-4.3**, **Fig. 4-4.3**, and **Fig. 5-4.3**, for wind characteristics #1 through #4 in the test matrix, respectively.



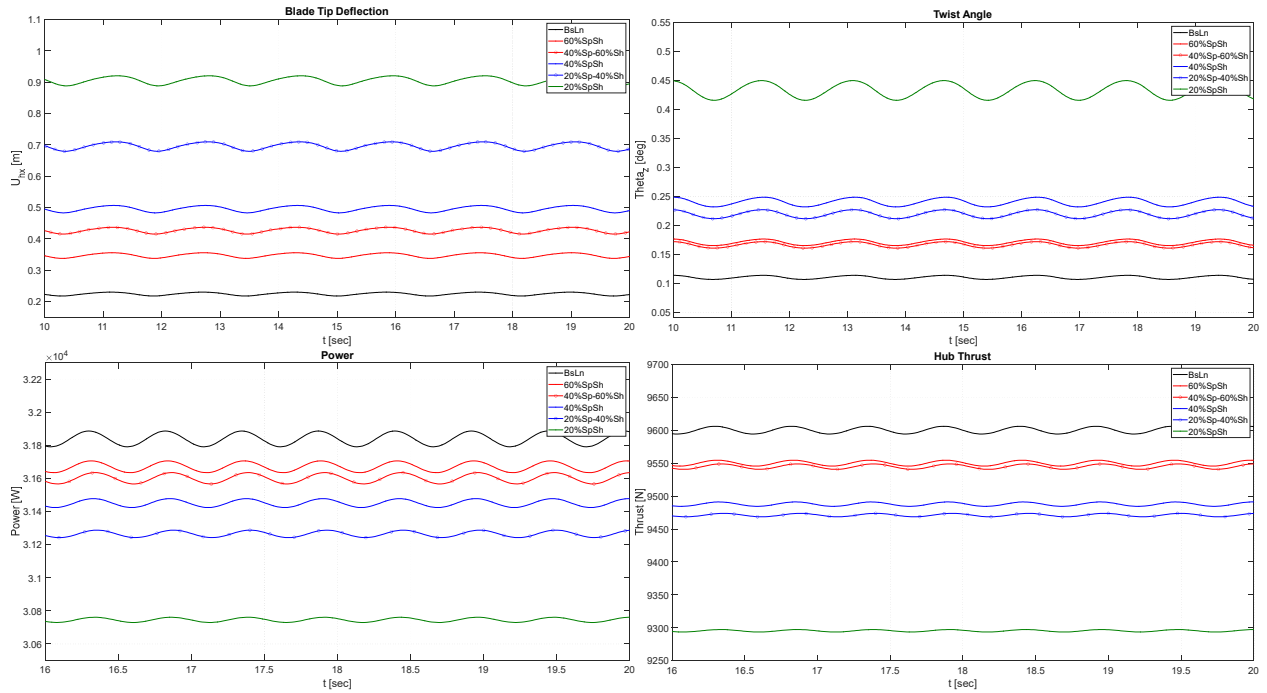


**Fig. 2-4.3:** Aeroelastic oscillatory behavior for the NRT Baseline blade, and its flex variations. Matrix Condition #1: Day, WS 6m/s, shear exp. = 0.06, yaw offset =  $0^\circ$ , TSR = 9, veer =  $0^\circ$

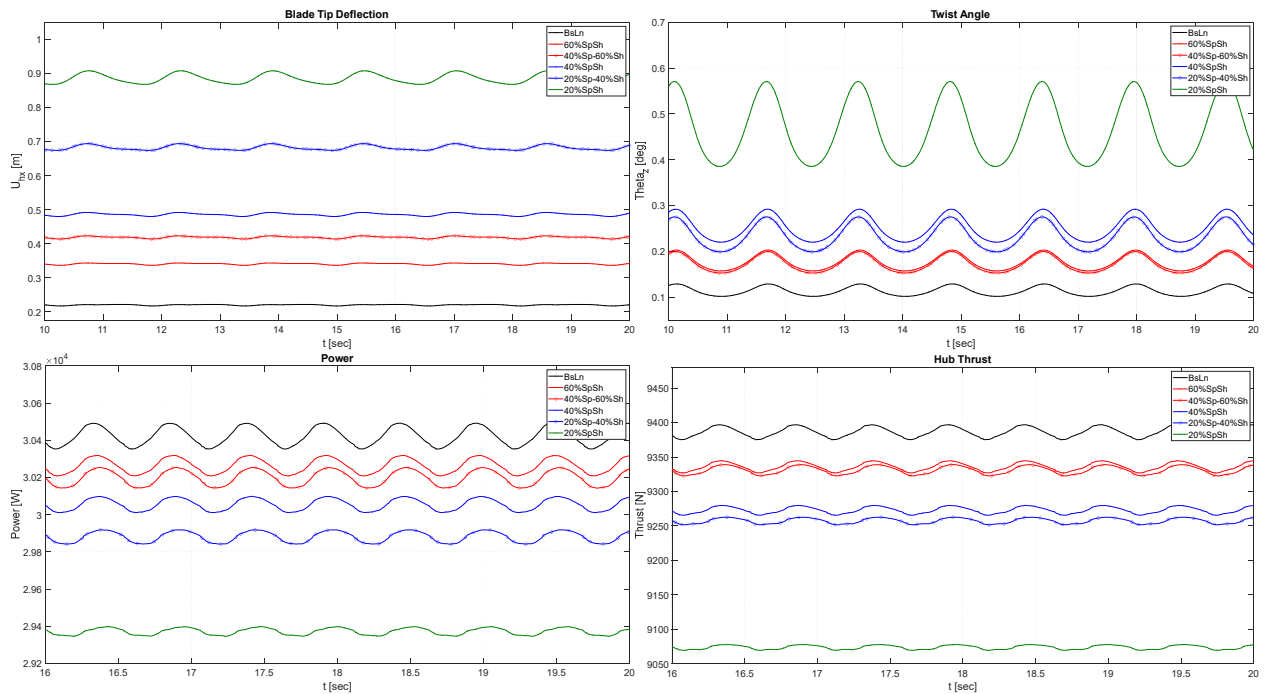


**Fig. 3-4.3:** Aeroelastic oscillatory behavior for the NRT Baseline blade, and its flex variations. Matrix Condition #2: Day, WS 6m/s, shear exp. = 0.06, yaw offset =  $10^\circ$ , TSR = 9, veer =  $0^\circ$ .

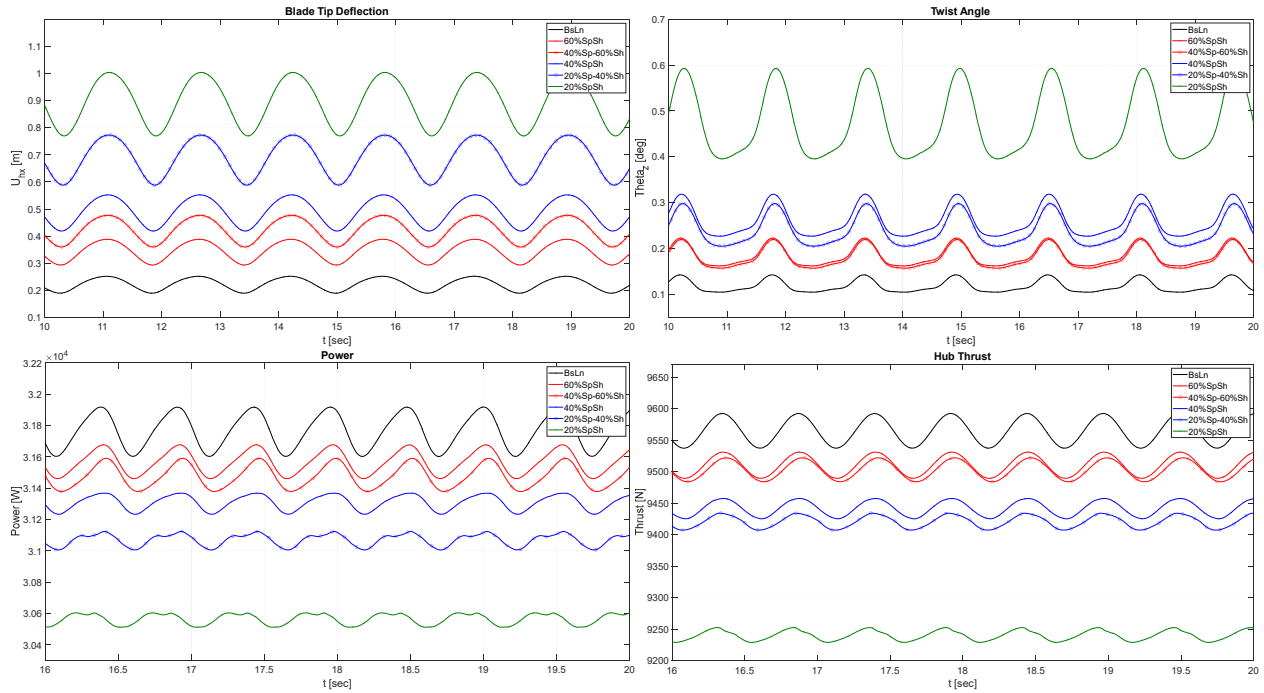


**Fig. 4-4.3:** Aeroelastic oscillatory behavior for the NRT Baseline blade, and its flex variations. Matrix Condition #3: Night, WS 6m/s, shear exp. = 0.30, yaw offset = 0°, TSR = 9, veer = 0°.

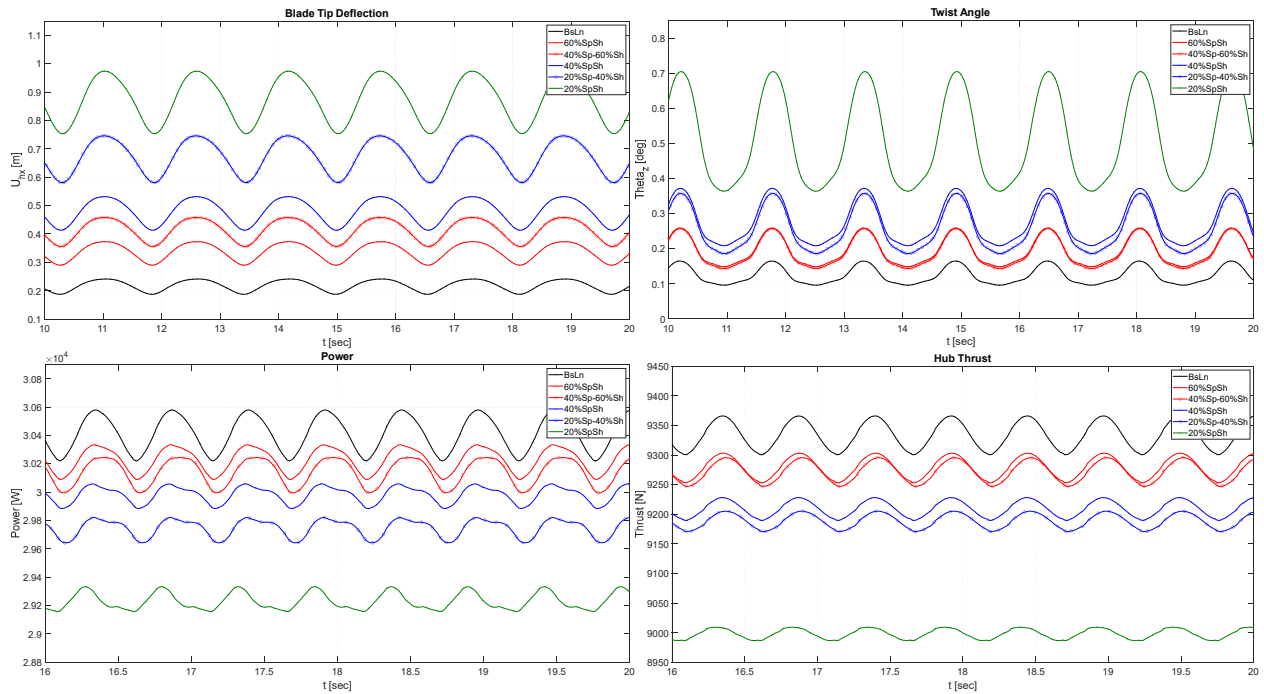


**Fig. 5-4.3:** Aeroelastic oscillatory behavior for the NRT Baseline blade, and its flex variations. Matrix Condition #4: Night, WS 6m/s, shear exp. = 0.30, yaw offset = 10°, TSR = 9, veer = 0°

### Third Stage - Vortex Wake Structure and Wake Velocity Patterns:










CODEF-GVLM solutions were computed for the NRT baseline blade and its flexible variations (b), (d), and (f), operating at daytime conditions without yaw and nighttime conditions with yaw (i.e., wind characteristics #1 and #4 in the test matrix). Based on the results of the tests on the rotor’s aeroelastic response obtained previously, these combinations of flex variations and case scenarios were selected as those which were likely to show the most significant changes in vortex wake structure and wake velocity patterns.

**Fig. 6-4.3** and **Fig. 7-4.3** show perspective views of the vortex-lattice meshes produced by GVLM which serve to illustrate the differences in vortex-wake structure between the baseline blade and the (b), (d), and (f) flex variations. **Fig. 6-4.3** shows a close-up view of the rotor and the near wake, and **Fig. 7-4.3** a full view of the wake up to 7D downstream of the rotor. **Fig. 8-4.3** shows a cross-cut rear view of the vortex-lattice mesh at 4D downstream of the rotor.

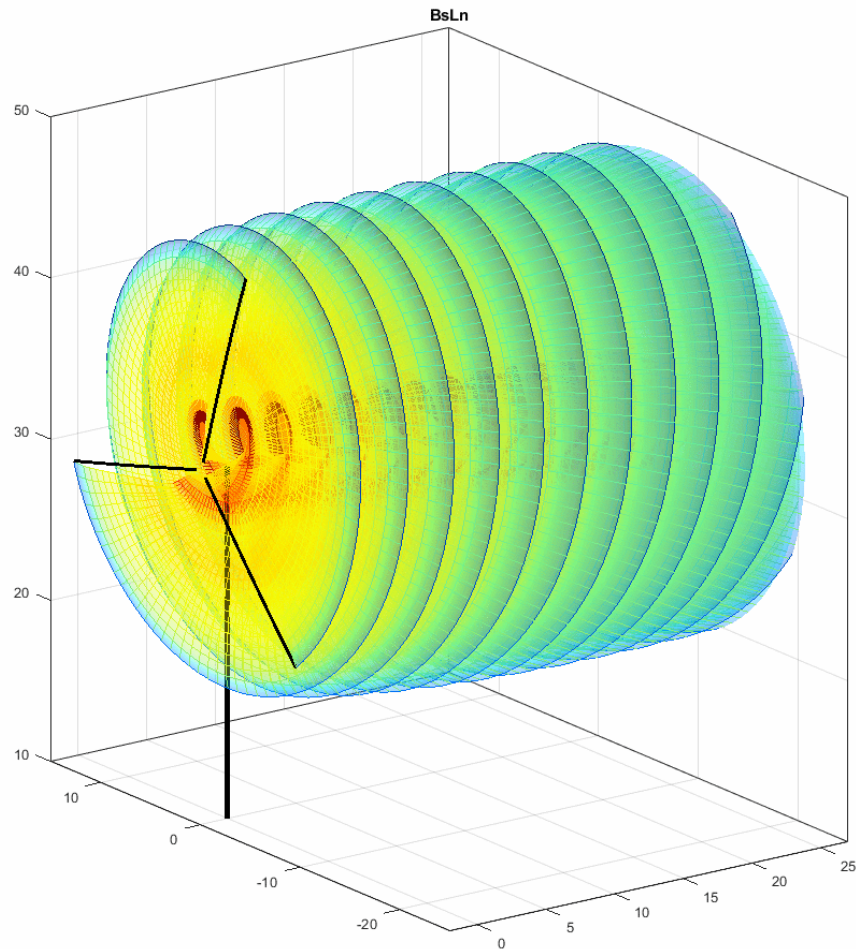
These vortex-lattice images are followed by perspective views of the velocity patterns at cross-sectional planes distributed along the longitudinal axis of the wake, from a distance of 1D downstream of the turbine to 7D. The planes were separated at intervals of 1D along the zone spanning the wake length. **Fig. 9-4.3** and **Fig. 10-4.3** show examples of perspective views of the velocity patterns on the cross-sectional planes for the case of the baseline blade rotor, operating at Matrix Condition #1 and Matrix Condition #4 respectively.

The velocity pattern plots are followed by perspective views of the wake velocity difference between the baseline case and each of the three selected flexible variations, normalized by the value of the incident wind. **Fig. 11-4.3** shows the case of Matrix Condition #1, and **Fig. 12-4.3** the case of Matrix Condition #4. These velocity difference maps were computed on the same cross-sectional planes up to 7D downstream, in 1D increments. The first image on each figure shows a perspective view case for the BsLn-60%SpSh comparison, followed below by a sequence of individual frames corresponding to the cases for the BsLn-60%SpSh, BsLn-40%SpSh, and BsLn-20%SpSh comparisons. Each of the three columns correspond to a case. The color scale is in [%] difference versus the undisturbed incident wind.

In order to provide a better visualization of the vortex wake structures, **Fig. 6-4.3**, **Fig. 7-4.3**, **Fig. 8-4.3**, **Fig. 11-4.3**, and **Fig. 12-4.3** are all linked to corresponding animated plots of the same patterns, included in **Appendix 1**. The corresponding links can be activated by pressing the “Play” icons located in the figure captions. After watching, the reader can return to the main text by pressing an icon at the bottom of the corresponding animated plot. All animated plots are provided with control features to play at different speeds, to pause, or to navigate one frame at a time. The key to operating these controls is listed in **Table 2-4.3**.

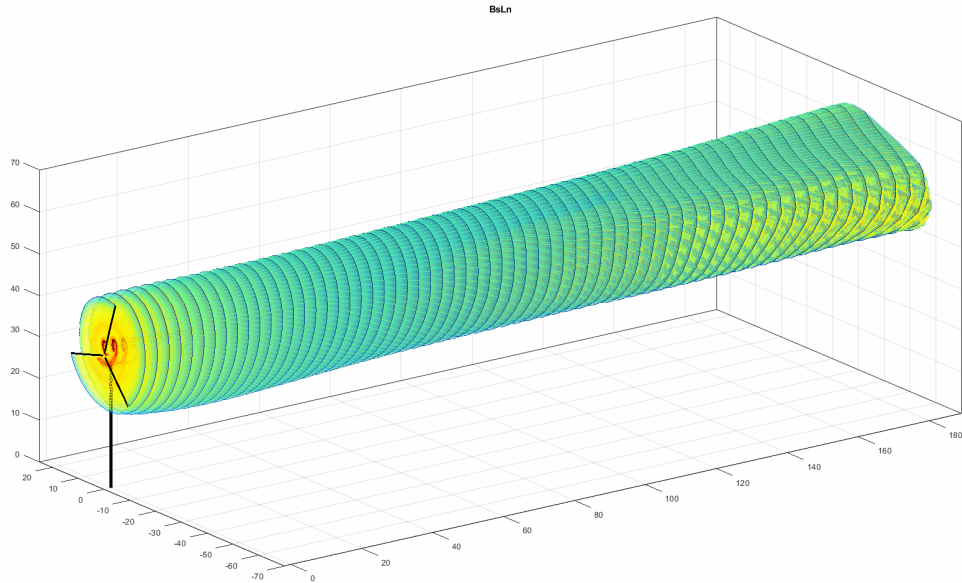
|  |   |  |
|--|---|--|
|  Play (1x Speed)  |  Pause   |  Stop   |
|   0.5x/2x Play Speed |   Previous/Next Frame |   First/Last Frame |

**Table 2-4.3:** Key to the operating controls for all the animated graphs included in this report.



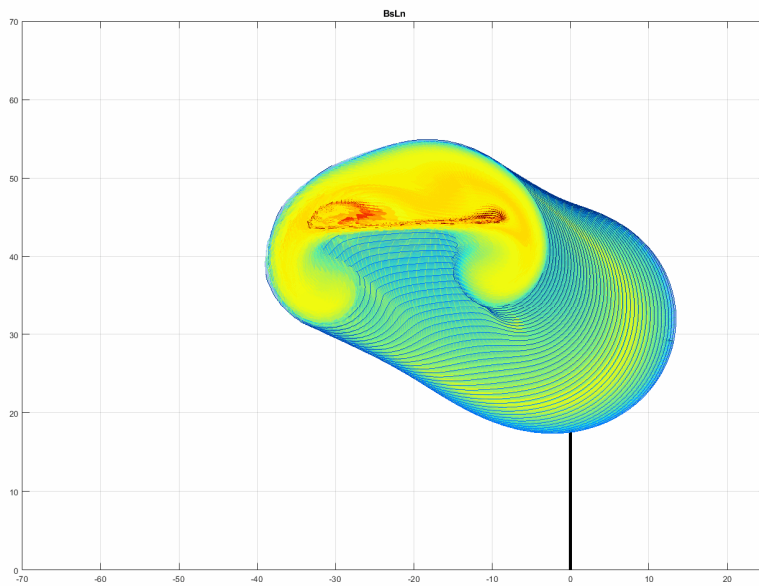
▶ Play

**Fig. 6-4.3:** Close-up perspective view of the vortex wake structure. Matrix Condition #4: Night, WS 6m/s, shear exp. = 0.30, yaw offset = 10°, TSR = 9, veer = 0°. Image shows the case for the BsLn blade. Clicking on the Play icon will open an animated plot showing in a sequence the cases for the BsLn, 60%SpSh, 40%SpSh, and 20%SpSh blades, which allows to see the relative change in blade deflection due to the difference in flexibility, and its effect in the generation of vortex filaments.



▶ Play

**Fig. 7-4.3:** Perspective view of the vortex wake structure up to 7D downstream. Matrix Condition #4. Image shows the case for the BsLn blade. Clicking on the Play icon will open an animated plot showing in a sequence the cases for the BsLn, 60%SpSh, 40%SpSh, and 20%SpSh blades.



▶ Play

**Fig. 8-4.3:** Cross-cut rear view of the vortex wake structure at 4D downstream. Matrix Condition #4. Image shows the case for the BsLn blade. Clicking on the Play icon will open an animated plot showing in a sequence the cases for the BsLn, 60%SpSh, 40%SpSh, and 20%SpSh blades.

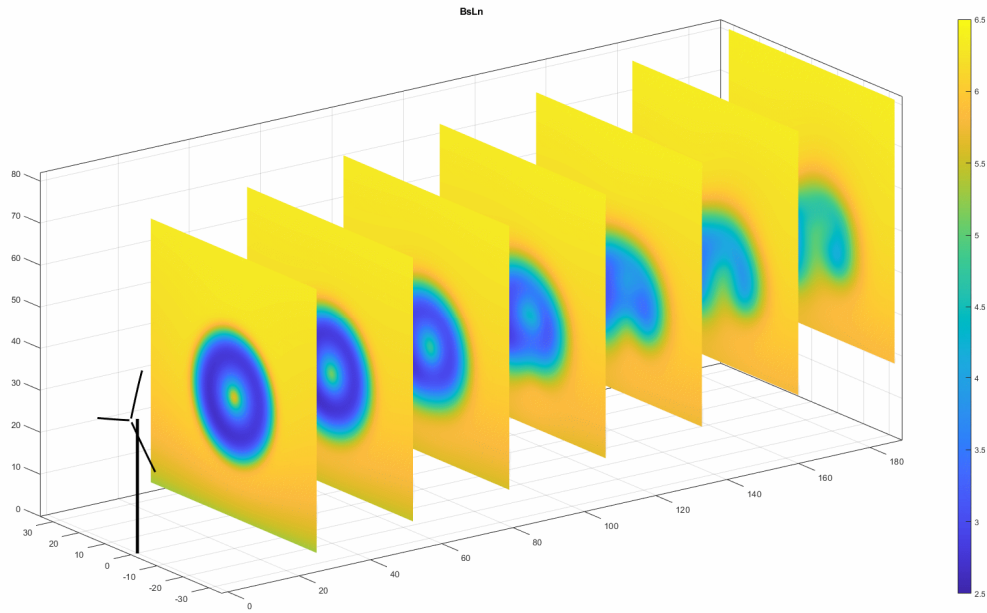


**Fig. 9-4.3:** Perspective view of wake velocity maps on cross-cut sections up to 7D downstream, in 1D increments. Matrix Condition #1: Day, WS 6m/s, shear exp. = 0.06, yaw offset = 0°, TSR = 9, veer = 0°. Image shows the case for the BSLn blade. Velocity scale is in [m/s].

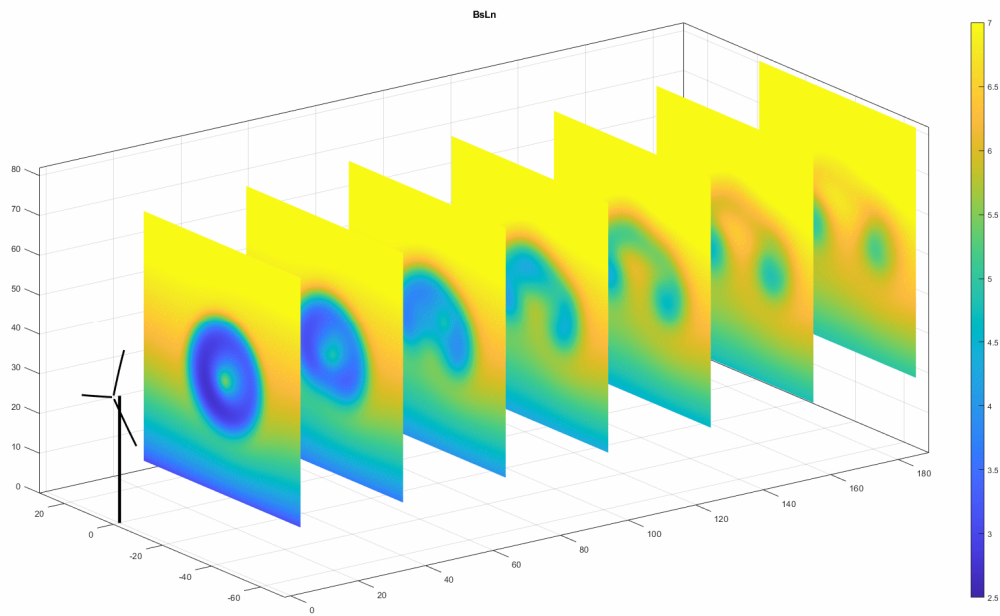
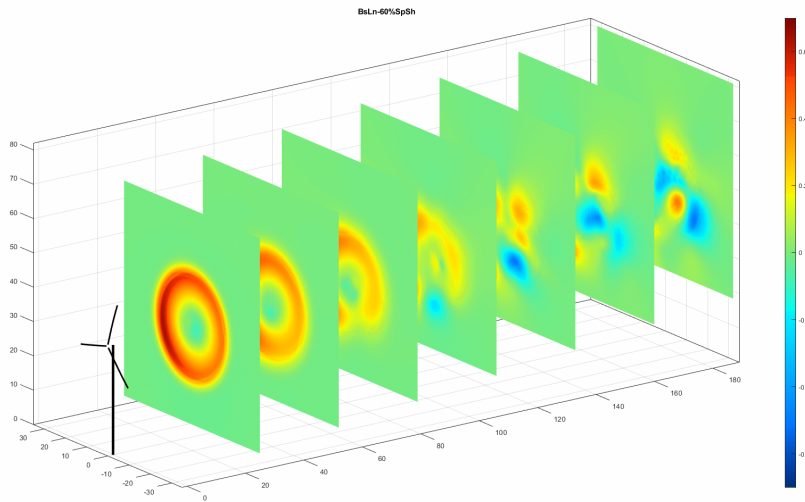
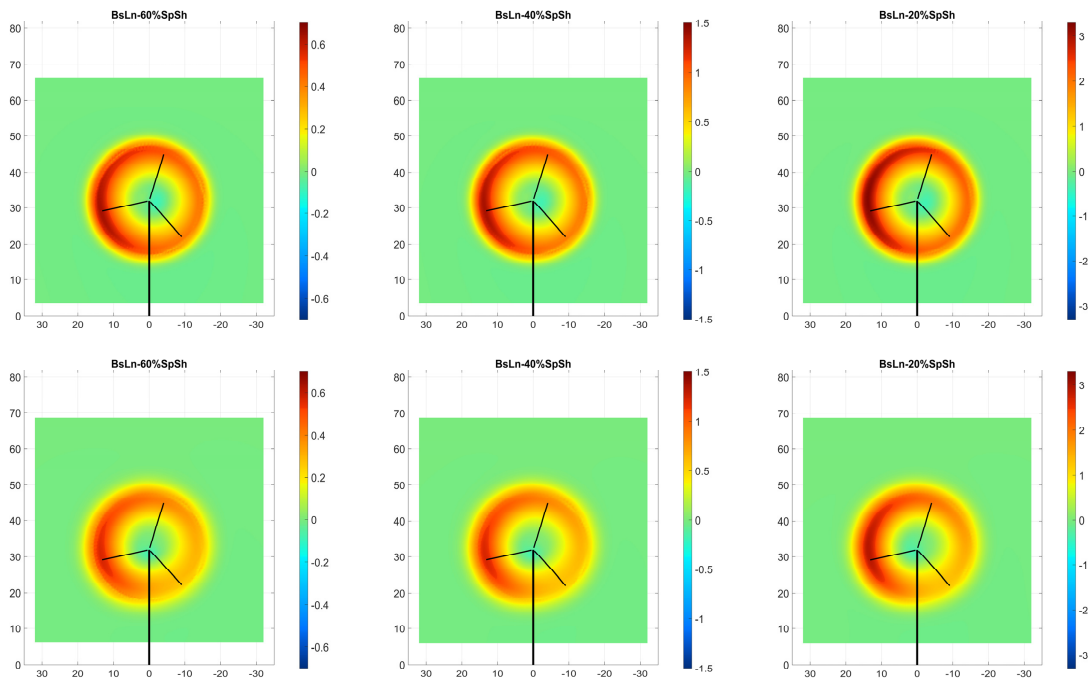


**Fig. 10-4.3:** Perspective view of wake velocity maps on cross-cut sections up to 7D downstream, in 1D increments. Matrix Condition #4: Night, WS 6m/s, shear exp. = 0.30, yaw offset = 10°, TSR = 9, veer = 0°. Image shows the case for the BSLn blade. Velocity scale is in [m/s].



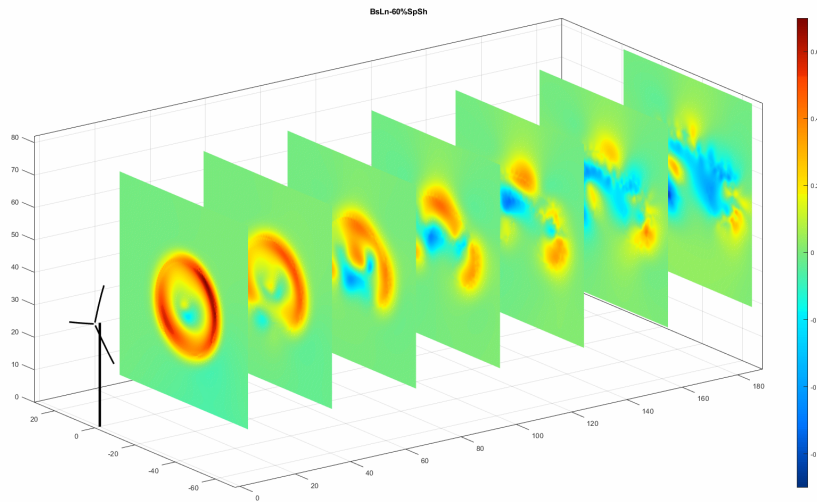
▶ Play

**Fig. 11-4.3:** Perspective view of maps of wake velocity difference between the BsLn case and its 3 flexible variations, plotted on cross-cut sections up to 7D downstream, in 1D increments. Matrix Condition #1. Image shows the case for the BsLn-60%SpSh comparison. Scale is in [%] difference versus the undisturbed wind. Clicking on the Play icon will open an animated plot showing in a sequence the cases for the BsLn-60%SpSh, BsLn-40%SpSh, and BsLn-20%SpSh comparisons. Below, the series of individual frames are shown, the 3 columns correspond to each case, and the 7 rows to the downstream distance of each cross-cut section.



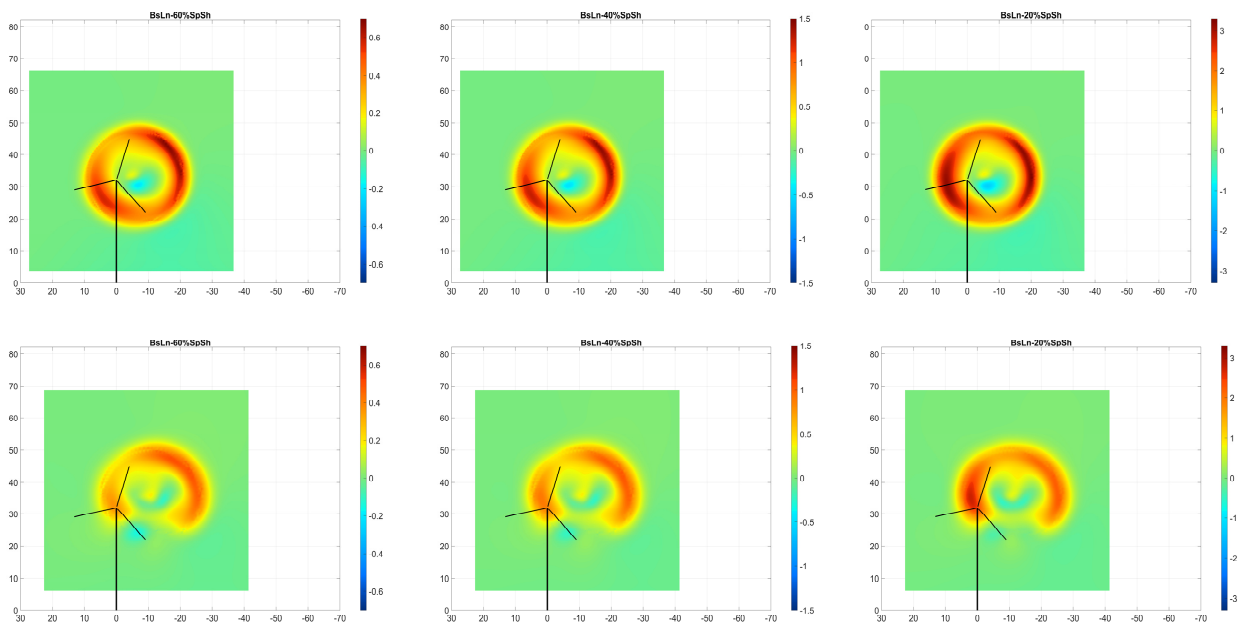


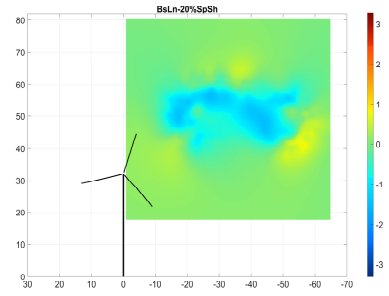
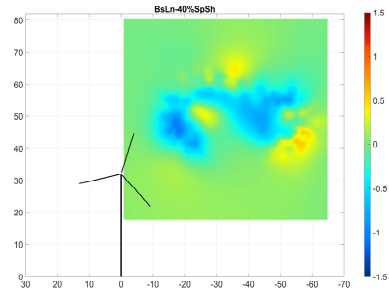
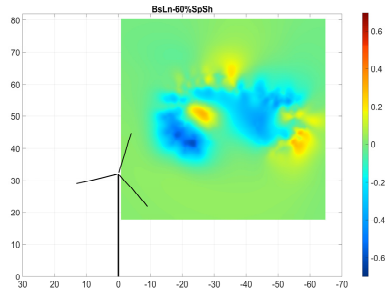
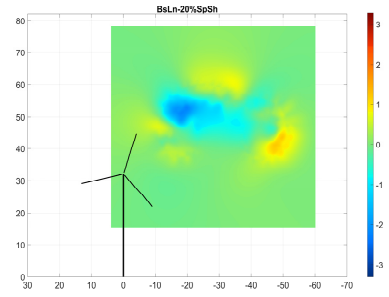
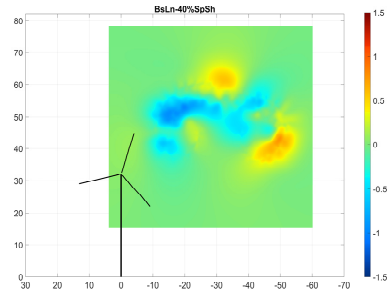
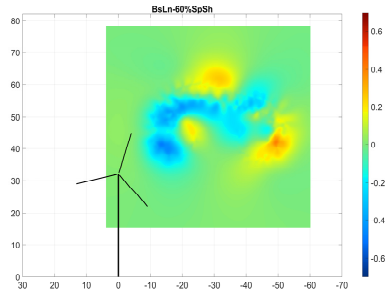
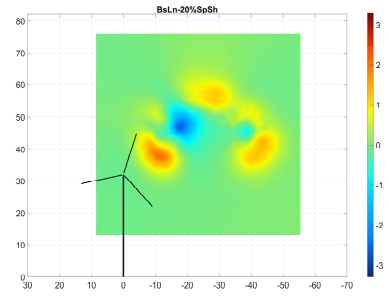
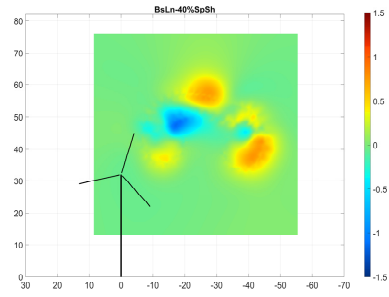
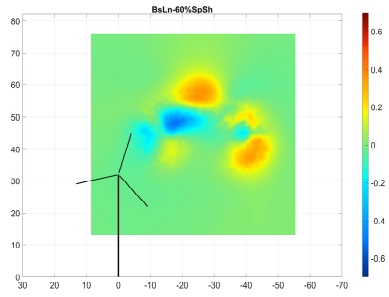
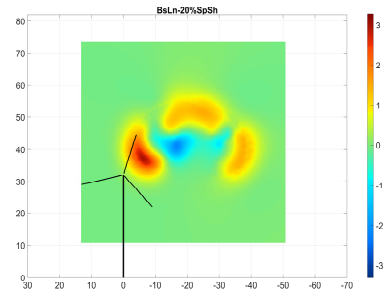
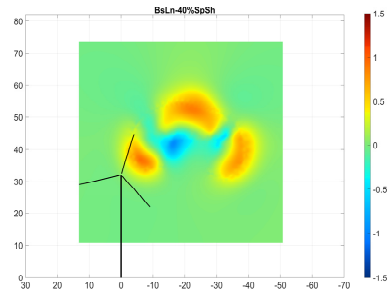
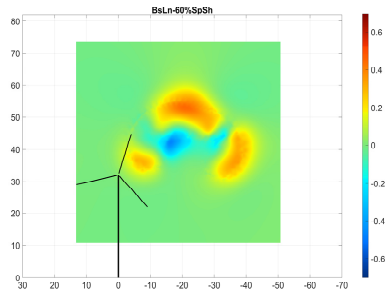
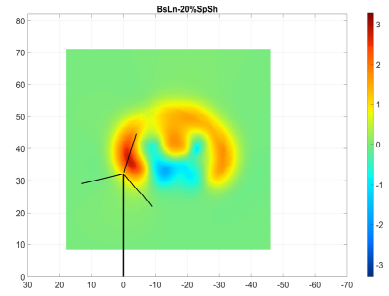
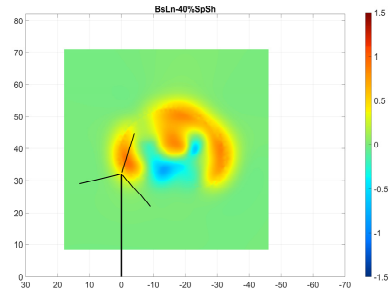
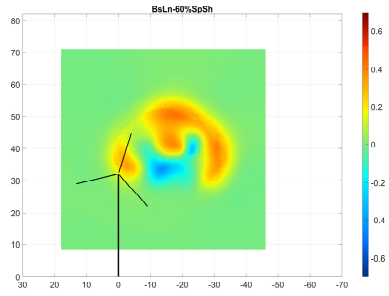




▶ Play

**Fig. 12-4.3:** Perspective view of maps of wake velocity difference between the BsLn case and its 3 flexible variations, plotted on cross-cut sections up to 7D downstream, in 1D increments. Matrix Condition #4. The image shows the case for the BsLn-60%SpSh comparison. Scale is in [%] difference versus the undisturbed wind. Clicking on the Play icon will open an animated plot showing in a sequence the cases for the BsLn-60%SpSh, BsLn-40%SpSh, and BsLn-20%SpSh comparisons. Below, the series of individual frames are shown, the 3 columns correspond to each case, and the 7 rows to the downstream distance of each cross-cut section.





## 5. Concluding Remarks

From the shared data, which described the constructive characteristics of the NRT baseline blade including airfoil shapes, spanwise distribution of geometrical and structural properties, internal structure layout, and materials, blade characteristics were translated into MTU's multiphysics CODEF format. Then, a preliminary First Stage series of results was obtained for the aeroelastic oscillatory response of the NRT baseline blade, and that had their spar-caps reduced by 80% and 90%. The time evolution of several variables that illustrate the structural response when exposed to the daytime and nighttime flow patterns were examined. In particular, the blade-tip deflection, torsional angle, angle of attack and aerodynamic loads at some representative blade sections, and power, torque and thrust at the hub were reviewed.

From those preliminary results, the Second Stage of the research work involved a complete revision of the materials and thicknesses of different components of the internal structure, exploring alternative ways of softening the blade by scaling the thicknesses of those components. Focus was given to the 80% thickness reductions to emphasize the effects of the contribution of different members of the internal structure, with the intention of exploring other percentage variations later on.

A strong shell contribution to the overall stiffness of the NRT blade was found, emphasized by an addition of unifilar material to the bilinear layers of the shell structure, located in the region of the span between 7% and 20% from the root. At its peak, around the 11% and 13% stations, these layers of unifilar material were quite substantial in proportion to the total of unifilar spar-cap material thickness. Thus, in the variations created, cases were added where that portion of shell unifilar material is also reduced together with the spar-cap. Combinations of thickness reductions in the shell as a whole were also tried, as well as thickness reductions in the shell plus the spar-cap.

A summary description of the different blade structural variations tested in this Second Stage was reported, including plots of the three basic stiffnesses and blade-mass span distributions for the variations, compared with the baseline blade. Those were followed by plots of the time evolution of the blade aeroelastic and hub variables, when operating in the daytime and nighttime wind scenarios. Results from vortex-wake simulations for these 80% flexible variations were also reported, and compared with the baseline blade case.

During the Third Stage, five new blade variations of increased flexibility were created, combining different scaling factors for the spar cap and the shell thicknesses. Their aeroelastic response was analyzed in four different wind scenarios: daytime and nighttime, with and without yaw. Vortex-lattice structure and wake velocity patterns for the three variations showing the most significant changes in aeroelastic response were also analyzed. Patterns were plotted at different locations up to seven rotor diameters downstream of the turbine, for two wind scenarios: daytime no-yaw, and nighttime with yaw. These represent the ends of the spectrum in terms of the cyclical variations that they induce in the aerodynamic loads. The difference in wake axial velocity between the baseline blade and each one of those three flexible variations were reported, normalized by the value of the incident wind. They have shown maximum

percentage variations between 1 % and 3.5 %, with various distributions in the locus of the pattern of velocity difference.

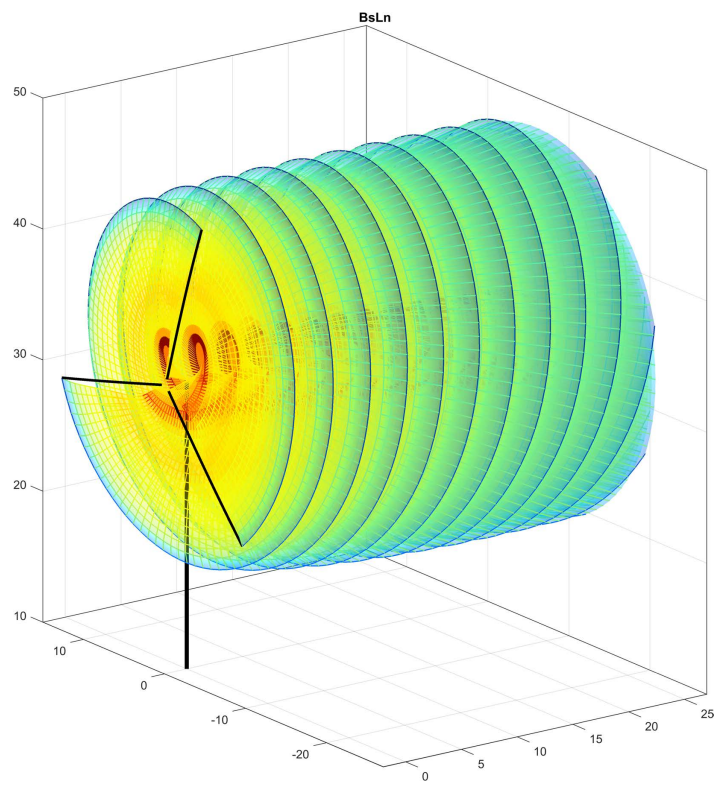
As an outlook for further work, it was observed that, in the Steady-In-The-Average (SITA) wind conditions cases analyzed during this phase of the project, the stimuli of the aerodynamic load fluctuations come from the cyclical motion of the blades traversing through a variable flow field caused by wind shear, tilt, and yaw. In these SITA cases, the frequency of fluctuations is mostly dominated by the rotor's turning speed, which is comparatively slow versus other stimuli. It could be hypothesized that differences in dynamic response between the baseline blade and its more flexible variations would likely become more intense when rapid temporal fluctuations, based on anemometry data, were added to the input wind. This would be due to the fact that the different natural frequencies on the aeroelastic response of the blade's flex variations will be triggered by the short-term pulses in the wind signal, impacting the wake structure more intensely. This will substantially affect the vortex-shedding process, altering the wake patterns of each of the different blade types. This aspect will certainly be worth testing as part of the next phase of the project, which will be part of a following report.

## References:

- [1] F. Ponta, A. Otero, L. Lago, A. Rajan (2016); "Effects of Rotor Deformation in Wind-Turbine Performance: The Dynamic Rotor Deformation Blade Element Momentum model (DRD-BEM)"; *Renewable Energy*, Elsevier; Vol. (90), 157-170.
- [2] A. Otero, F. Ponta (2010); "Structural Analysis of Wind-Turbine Blades by a Generalized-Timoshenko Beam Model", *Journal of Solar Energy Engineering*, ASME; Vol. (132), 011015, 1-8.
- [3] F. Ponta, P. Jacovkis (2001); "A Vortex Model for Darrieus Turbine Using Finite Element Techniques"; *Renewable Energy*, Elsevier; Vol. (42), 1-18.
- [4] J. Strickland, B. Webster, T. Nguyen (1979); "Vortex Model of the Darrieus Turbine: An Analytical and Experimental Study"; *Journal of Fluids Engineering*, ASME; Vol. (101), 500-505.
- [5] F. Ponta, (2010); "Vortex Decay in the Karman Eddy Street"; *Physics of Fluids*, American Institute of Physics; Vol. (24), 093601, 1-11.
- [6] F. Ponta, H. Aref (2004); "Strouhal-Reynolds Number Relationship for Vortex Streets"; *Physical Review Letters*, American Physical Society; Vol. (93), 084501, 1-4.
- [7] F. Ponta (2006); "Analyzing the Vortex Dynamics in Bluff-Body Wakes by Helmholtz Decomposition of the Velocity Field", *Fluid Dynamics Research*, Elsevier; Vol. (38), 431-451.

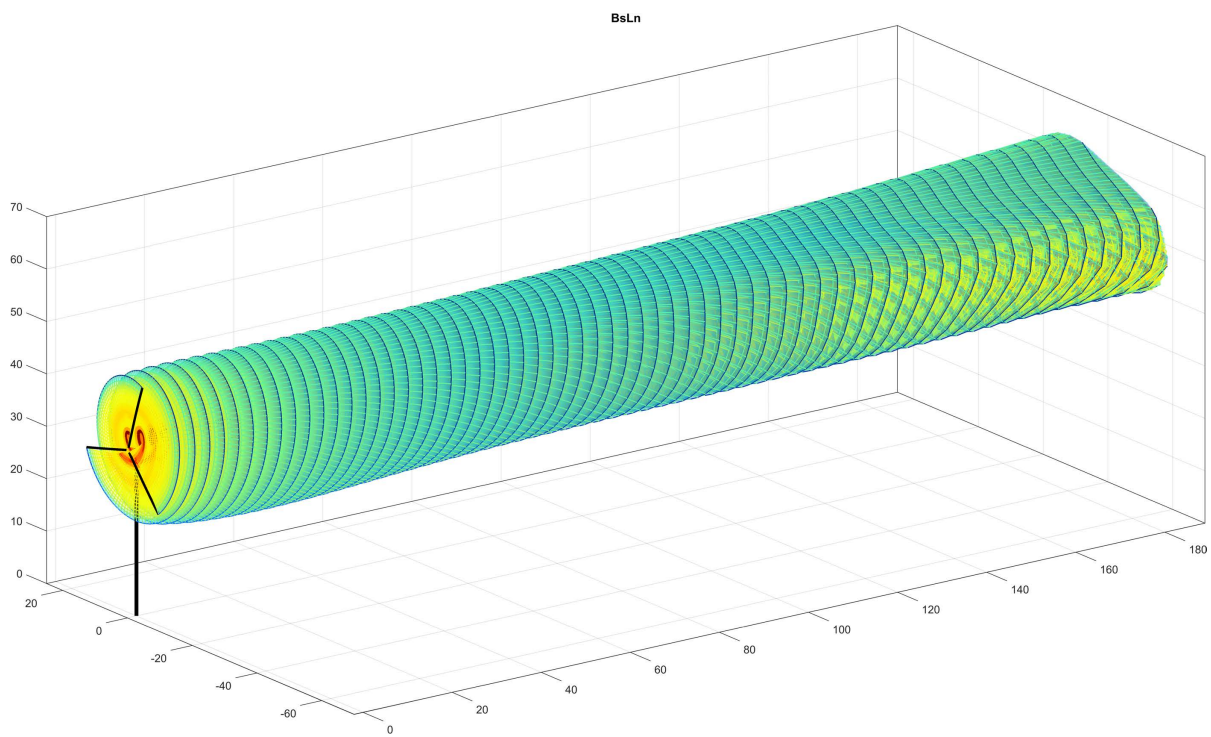
## Appendix 1

## Comparison of Vortex Lattices : Close-up view



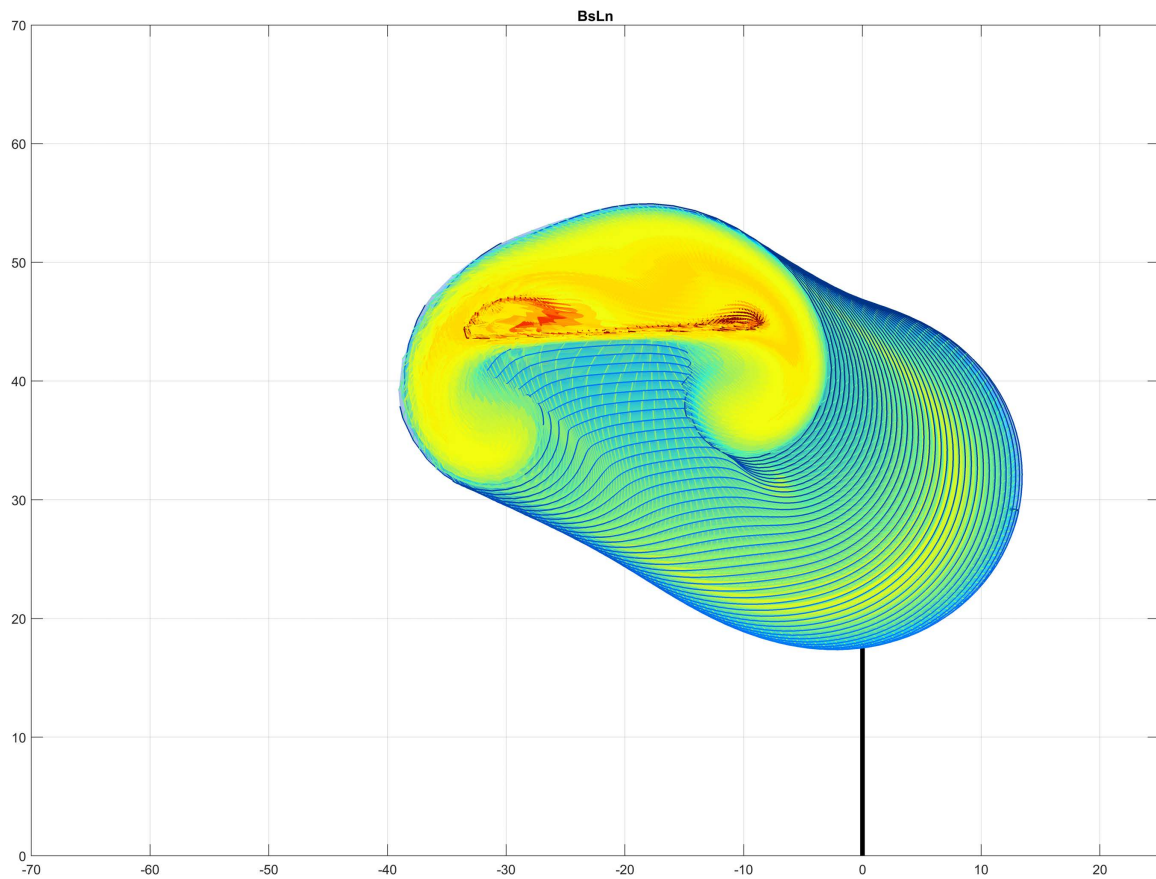
[Back to main text](#)

## Comparison of Vortex Lattices : Perspective view



[Back to main text](#)

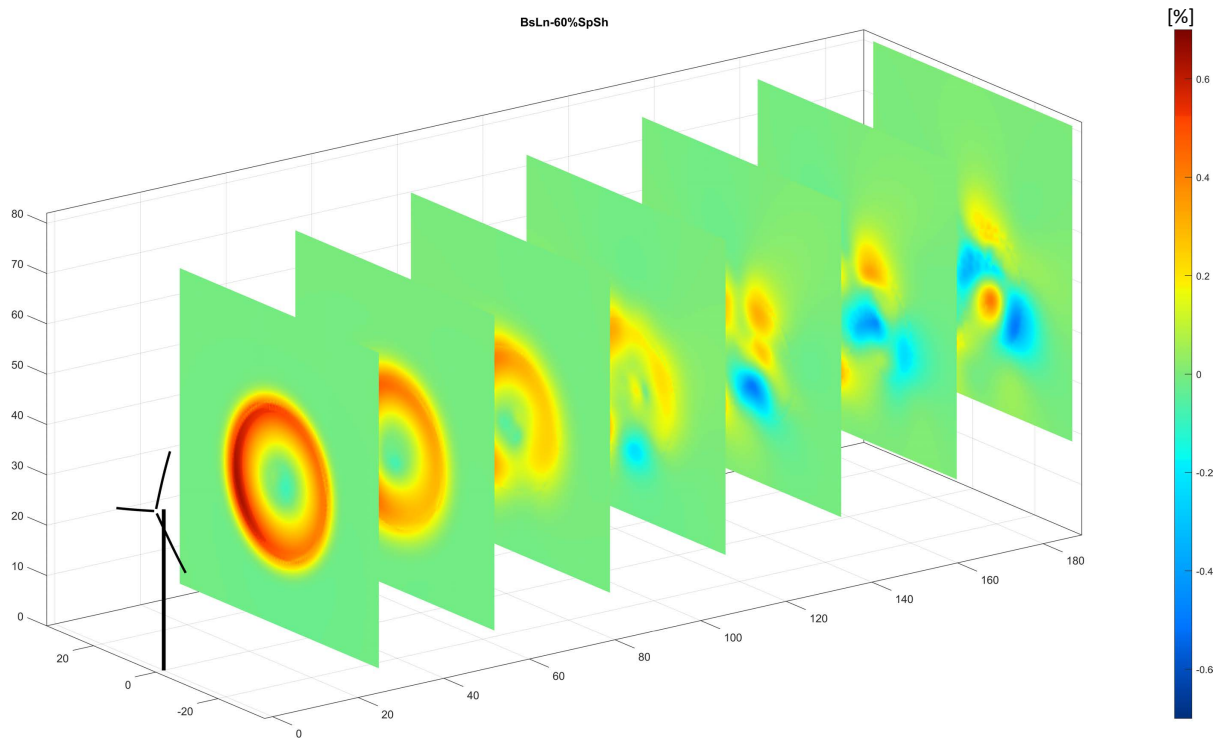
## Comparison of Vortex Lattices : Rear view



[Back to main text](#)

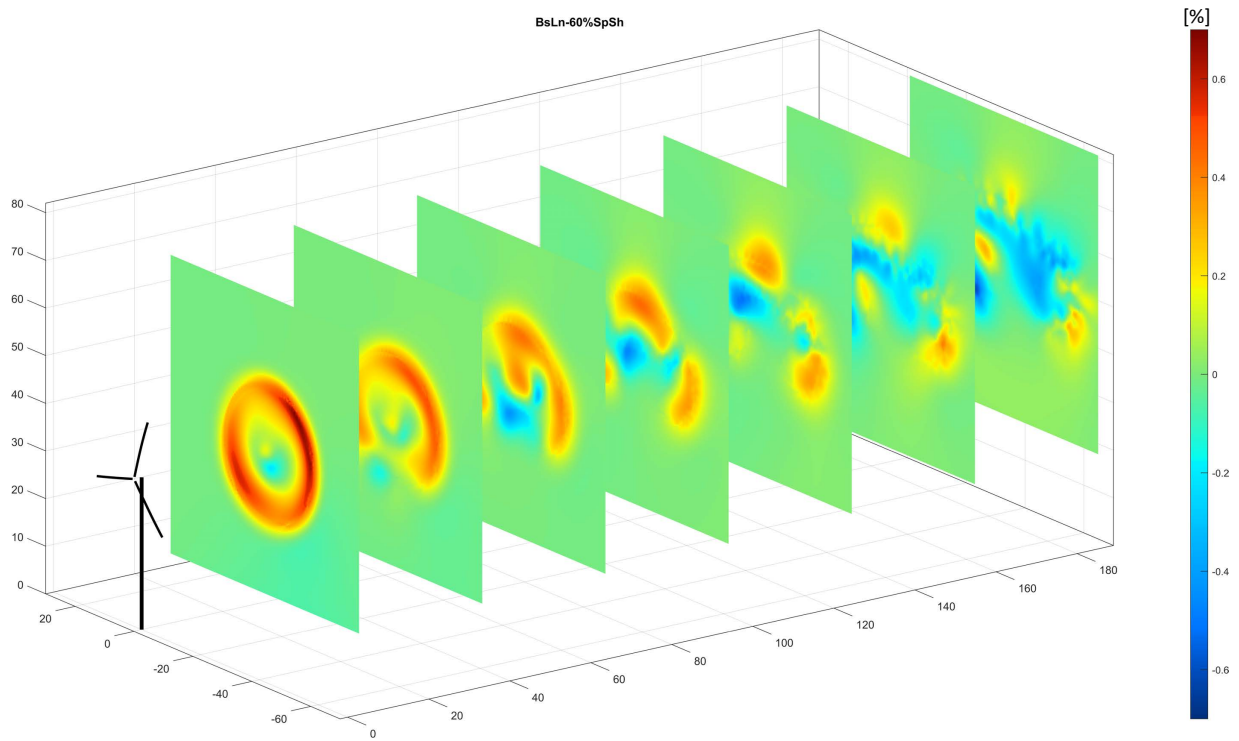


# Wake Velocity Difference - Matrix Condition #1



[Back to main text](#)

# Wake Velocity Difference - Matrix Condition #4



[Back to main text](#)